

---

# 8 Fractures

## 8.1 SURFACE CREVASSES

Most of the topics and applications discussed in this book deal with ductile behavior of ice resulting in continuous deformation or creep under comparatively low stresses. This is the primary mode of glacier motion and most relevant to glacier modeling. However, most people traveling on glacier surfaces will be struck by physical manifestations of the brittle nature of ice, namely, crevasses. Crevasses are imposing chasms cutting through the surface of most glaciers that form primarily under tension when stretching cannot be accommodated by ductile flow and, instead, the ice behaves as a brittle material susceptible to rupturing. Most crevasses are confined to the upper few tens of meters and do not importantly affect glacier flow. There are, however, several reasons why crevasse initiation and propagation has received some attention in the glaciological literature. First, the orientation of crevasses—usually perpendicular to the direction of principal tensile stress—may contain information about the regional stress field (c.f. Van der Veen, 1999a). Second, fracture propagation is the primary mechanism by which icebergs break off from glacier termini, and better understanding and quantification of this process may aid in formulation a calving relation for numerical models (Van der Veen, 2002; Benn et al., 2007a,b). Third, rapid downward propagation of water-filled crevasses may be a mechanism by which meltwater ponds formed at the glacier surface can almost instantaneously penetrate the full ice thickness, thus providing a drainage route for surface water to reach the glacier bed and provide additional lubrication (Van der Veen, 2007; Das et al., 2008). For these reasons, it is worthwhile to present a discussion of crevasses on glaciers based on the review of Van der Veen (1999a). The following sections in this chapter introduce the mathematical tools for modeling crevasses and fracture propagation on glaciers with application to iceberg calving.

Perhaps the earliest explanation for crevasses was given by Scheuchzer (1723), who suggested, in what has been characterized as poor medieval Latin, that crevasses formed during the summer as a result of expansion of air bubbles in the ice (Walker and Waddington, 1988). A century later, Hugi (1830) proposed that thermal stresses would generate crevasses during warm spells. While these earlier theories were soon proven to be incorrect, they appropriately recognized crevasses to be the product of stresses, or forces, acting on the ice. It was not long thereafter that these forces became identified with differential speed across the glacier surface, and by the 1840s it was generally accepted that “the formation of crevasses betokens a local distending force” (Forbes, 1859, p. 151). Similarly, Hopkins (1862, p. 706) concluded that “when the maximum normal tension is the force to which the cohesive power of a glacial mass first gives way, the result, as above observed, must be an open fissure,

or crevasse, the direction of which must manifestly be perpendicular to that of the tension producing it.”

In a paper presented May 1, 1843, at the Cambridge Philosophical Society (Hopkins, 1844a), the principles of force balance were outlined and used to find the orientation of principal stress acting on the surface of a glacier. Hopkins’s discussion is in terms of forces, but it is more appropriate to frame the discussion in terms of stresses. If  $A$  represents the normal stress directed along the horizontal  $x$ -axis (taken here to be the direction of flow, along the axis of the glacier),  $B$  the normal stress in the direction of the other horizontal  $y$ -axis, and  $F$  the tangential or shear stress in the  $xy$ -plane, the greatest normal tensile stress,  $P_1$  is given by

$$P_1 = \frac{1}{2} \left\{ A + B + \sqrt{(A - B)^2 + 4F^2} \right\}, \quad (8.1)$$

with its direction determined by

$$\tan 2\alpha = \frac{2F}{A - B}, \quad (8.2)$$

where  $\alpha$  represents the angle between the direction of  $P_1$  and the along-flow  $x$ -axis. As concluded in a second memoir (Hopkins, 1844b, art. 9), “The maximum action here spoken of is the maximum *tension* at the proposed point, and since it is perpendicular to the corresponding line of separation, *there will manifestly be the greatest tendency to form a fissure along that line, and a fissure will be formed along it if the maximum tension be greater than the cohesive power at the proposed point*” (ital. original). In other words, if the tensile stress,  $P_1$ , exceeds a critical value depending on the strength of ice, a crevasse (or fissure) will open perpendicular to the direction of  $P_1$ . In a later paper, Hopkins (1862) applied the above formulas to explain the orientation of crevasses as frequently observed on glaciers in the Alps.

Consider first a glacier descending a valley with approximately parallel sides so that the normal stress in the direction perpendicular to the flow direction may be neglected ( $B = 0$ ). Toward the margins the speed approaches zero and the dominant stress acting on the ice is the shear stress,  $F$ , representing lateral drag due to resistance offered by the rock walls. Setting  $A = 0$  in equation (8.1) gives the principal tensile stress,  $P_1 = F$ , while equation (8.2) yields an angle of  $45^\circ$  with the axis of the glacier as the direction of principal tensile stress. Thus, near the margin, crevasses will strike at  $45^\circ$ , as in region I in Figure 8.1. Near the centerline of the glacier, on the other hand, the effect of drag from the margins is negligible ( $F = 0$ ), and the stress responsible for crevasse opening is the normal tensile stress,  $A$ , acting along the flow axis so that crevasses open perpendicular to this axis (region II in Figure 8.1). Where the valley walls diverge, longitudinal or splaying crevasses may form. From continuity arguments it follows that the speed along the  $x$ -axis must decrease as the ice spreads laterally, and  $A$  becomes negative (compressive) while the other normal stress,  $B$ , is positive (tension). Where this tensile stress becomes sufficiently large, fracturing in the direction of the glacier axis will occur. The diverging flow causes

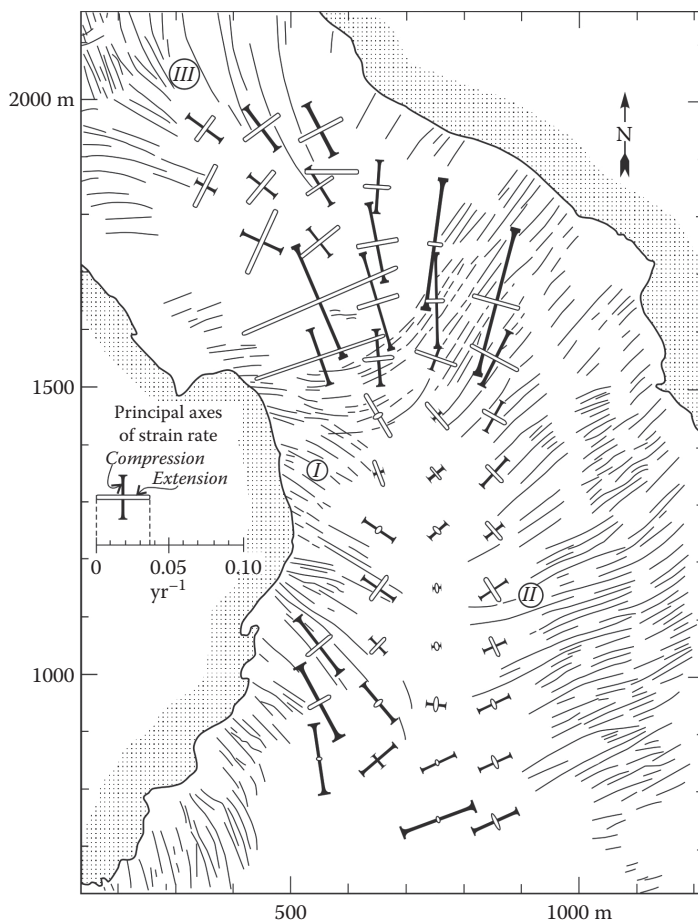


**FIGURE 8.1** Principal surface strain rates and crevasse orientation on Blue Glacier, Olympic Mountains, Washington state. Ice flow is toward the top of the figure. (From Meier, M. F. et al., *J. Glaciol.*, 13, 187–212, 1974. Reprinted from the *Journal of Glaciology* with permission of the International Glaciological Society and the authors.)

these crevasses to splay radially, resulting in the pattern near the top in Figure 8.1 (region III).

The patterns predicted by Hopkins's model conform in many instances with those observed on glaciers. There are exceptions, however, in particular where crevasses meet glacier margins. For example, on Blue Glacier shown in Figure 8.1 near the margin opposite region I (below the North arrow), crevasses strike the margin at angles approaching  $90^\circ$ . Without considering in detail the stress distribution in relation to crevasse orientation, the causes for such deviations from predictions cannot be identified. Careful testing of the Hopkins model is possible for those glaciers on which surface strain rates (velocity gradients) were measured and crevasse patterns mapped. Several such studies are summarized in Van der Veen (1999a). Generally,

crevasses appear to form in a direction close to perpendicular to the direction of principal tensile strain but there are exceptions (for example, Zumbege et al., 1960; Kehle, 1964; Hambrey and Müller, 1978; Whillans et al., 1993). Some authors disregard differences between prediction and observation, based either on measurement uncertainties, on the fact that observed crevasses may have formed upglacier and rotated by the ice flow, or on the suggestion that not all crevasses are visible. In other words, the Hopkins model for crevasse formation has not yet been unambiguously tested, but it continues to be accepted. Those studies in which quantitative estimates of crevasse rotation are made conclude that these estimates do not agree with observations. Further, some crevasses show signs of strike-slip faulting, in which the two walls move parallel to each other, with displacements that can be much larger than the opening rate (for example, Kehle, 1964; Hambrey, 1976). Finally, crevasse traces persist over much greater distances and well into the ablation area, instead of being melted away completely, as would be expected for crevasse depths of several tens of meters.

A difficulty inherent in comparing theoretical crevasse orientation with observations is that until recently, no attempts were made to measure stresses on glaciers directly (first results of direct measurements of stress at depth in Worthington Glacier, Alaska, are described in Pfeffer et al., 2000). Instead, crevasse orientations are compared to the directions of principal strain or strain rate, because these quantities are readily measured on the surface of a glacier. That is, crevasses are assumed to form in the direction of the principal tensile strain rate. However, this direction need not coincide with the direction of principal tensile stress. As pointed out by Ambach (1968), strain rates may not be the best indicator for crevasse studies, as the principal stresses are not simply scaled to the principal strain rates. If  $\dot{\epsilon}_1$  and  $\dot{\epsilon}_2$  represent the two principal components of strain rate, the principal components of the full stress are (Nye, 1959, p. 416)

$$\sigma_1 = 2\eta\dot{\epsilon}_1 + \eta\dot{\epsilon}_2, \quad (8.3)$$

$$\sigma_2 = \eta\dot{\epsilon}_1 + 2\eta\dot{\epsilon}_2, \quad (8.4)$$

with

$$\eta = B\dot{\epsilon}_e^{1/n-1}, \quad (8.5)$$

the effective viscosity in the flow law for glacier ice linking stresses to strain rates. In this last expression,  $B$  represents the viscosity parameter,  $n = 3$  the flow-law exponent, and  $\dot{\epsilon}_e$  the effective strain rate (the second invariant of the strain-rate tensor). These relations show that even if one of the principal strain rates is tensile, the corresponding principal stress does not need to be tensile also (namely, when the value of the compressive strain rate is twice that of the tensile strain rate,  $\dot{\epsilon}_2 = -2\dot{\epsilon}_1$ ). The directions of the principal full stress and those of the principal strain rates are co-aligned so the orientation of crevasses is not affected by considering strain rates, rather the observational criterion for when crevassing first occurs.

Almost certainly, some criterion exists for crevasse initiation on glaciers, but there is disagreement in the literature as to what this criterion is. Meier (1958) and Vornberger and Whillans (1990) argue that crevasses form when the tensile principal *strain rate* reaches a threshold value. Other authors have proposed that crevasses are formed where the tensile *stress* reaches a critical value. Vaughan (1993) considered crevassing on 17 polar and alpine glaciers for which strain rates were available. Converting these strain rates to stresses using the constitutive relation for glacier ice, he derived failure envelopes suggesting that the tensile stress required for crevasses to form varies between 90 and 320 kPa. This range in required tensile stress is not caused by differences in ice temperatures but may reflect variations in ice properties that affect the strength of ice or, perhaps, by different crevasse spacings.

Early theories to estimate crevasse depth (Nye, 1955, 1957) made the assumption that crevasses penetrate to the depth at which the net longitudinal stress is zero, that is, where the longitudinal tensile stress equals the compressive ice overburden pressure. This model assumes zero cohesive strength of the ice and that crevasses can exist for all positive values of the tensile stress. The tensile stress tending to open a crevasse is the resistive stress,  $R_{xx}$ , defined in Section 3.1 as the full stress minus the weight-induced lithostatic stress,  $L$ . The depth,  $d$ , of the surface crevasse then follows from the requirement that

$$R_{xx}(d) = \rho g d, \quad (8.6)$$

where the right-hand side represents the lithostatic stress. Taking the stretching stress constant with depth, and assuming constant density, the crevasse depth can be estimated from

$$d = \frac{R_{xx}}{\rho g}. \quad (8.7)$$

For a typical stress of 150 kPa, this expression predicts a crevasse depth of about 17 m, using a constant density  $\rho = 917 \text{ kg/m}^3$  corresponding to solid ice. Generally, the density of the upper firn layer is considerably smaller than this value. Accounting for lower near-surface density is straightforward and, for a given stretching stress, would result in greater crevasse depth than that predicted by equation (8.7).

Nye's zero-stress model for estimating crevasse depth does not account for stress concentrations that may exist at the tip of the crevasse. This is a reasonable approximation for closely spaced crevasses because the tensile stress is nonexistent in the slabs separating neighboring crevasses. However, for single crevasses or those that are spaced sufficiently far apart so as to not affect stresses around neighboring crevasses, stress concentrations must be taken into account. Weertman (1973b) presents a model based on dislocation theory and finds that the depth of an isolated crevasse is greater than that predicted by equation (8.7) by a factor  $\pi/2$ . Again, a constant ice density is assumed in that model.

An alternative approach that can be applied to estimate the penetration depth of both single crevasses and of closely spaced crevasses is based on fracture mechanics

in which the strength of ice is described through the fracture toughness, or resistance to crack propagation. The application of fracture mechanics to crevasses on glaciers is the focus of the next section.

## 8.2 FRACTURE MECHANICS

Crevasse propagation on glaciers may, in good approximation, be described using procedures of linear elastic fracture mechanics (LEFM) (Smith, 1976, 1978; Rist et al., 1996; Van der Veen, 1998a). This approach is based on the assumption that solid materials contain small flaws and cracks that affect their load-bearing capacity. These cracks can grow to larger fractures if stress concentrations near the crack tip become large enough to overcome the material strength or cohesion of the material (Broek, 1986). LEFM applies only to materials that are brittle and for which inelastic deformation near the crack tip can be ignored. Because glacier ice is a viscous material that deforms under stress, for slow loading conditions, ductile processes acting at crevasse tips should be accounted for when modeling fracture growth. A formal treatment of ductile processes can be included, using the J-integral approach (Hutchinson, 1979) or path-independent  $C^*$  integrals (Riedel and Rice, 1980), but this would make the discussion much more complicated. In view of other uncertainties and approximations, a more complex theory of crevasse formation and propagation is not warranted for the present purposes. Because viscous properties of glacier ice make the strength of ice appear to be greater than if it were a true brittle material (Sanderson, 1988, p. 90), viscous effects can be accounted for by assigning a greater value to the fracture toughness. The LEFM approach is applicable provided the region near the crack tip where plastic deformation occurs is small compared with the depth of the crevasse (Gdoutos, 1993, p. 57). Following Broek (1986, p. 14), Van der Veen (1998a) estimates this plastic region to extend about 0.1–2.5 m from the crevasse tip, which is much less than the typical depth to which crevasses penetrate.

The fundamental assumption in the LEFM approach is that small starter cracks are present. Under suitable conditions, these cracks can grow into deeper fractures or crevasses. The initial crack size depends on the applied tensile stress. If the tensile stress is less than ~30 kPa, no crevasses can develop, while for stresses in the range of 40–60 kPa, an initial crack of 1–2 m depth is required. This initial depth decreases rapidly to a few cm for tensile stresses more common on glaciers and ice sheets (Van der Veen, 1999a). This requirement that a macroscopic initial crack must be present for crevasses to develop is a major weakness of the LEFM approach. On the scale of individual crystals, cracks could nucleate from dislocations or grain boundaries, and fracturing may result from crack nucleation or crack propagation; but on these microscopic scales, the concepts of stress intensity factor and fracture toughness may have limited applicability in the context as used here (Ingraffea, 1987). Modeling these microscopic processes is well beyond the scope of studies investigating crevasse propagation, and instead, the assumption is usually made that macroscopic cracks or flaws exist that can develop into full-fledged crevasses. In this respect, it should be noted that the fracture toughness of low-density snow and firn is orders of magnitude smaller than that of solid ice (Schulson and Duval, 2009). This opens the possibility that required starter cracks form from comparatively small

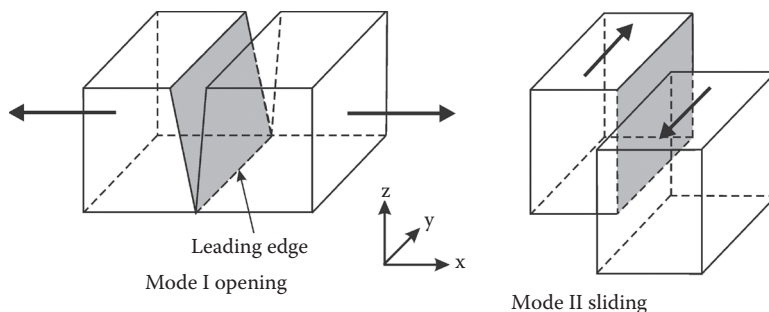


**FIGURE 8.2** Two principal modes of crack propagation. (Reprinted from Van der Veen, C. J., *Cold Regions Sci. Techn.*, 27, 31–47, 1998a. With permission from Elsevier.)

“flaws” in the firn (such as melt lenses or planes of structural weakness). Because of the smaller fracture toughness of firn, these flaws may propagate deeper than they could in solid ice and grow to deeper starter cracks that allow further downward propagation into more solid glacier ice.

Only one-dimensional Mode I fracturing is considered, with crevasses propagating downward perpendicular to a tensional stress (Figure 8.2). Other possibilities are the *sliding mode* (Mode II), resulting from shear in the plane of the fracture, and the *tearing mode* (Mode III), in which the applied shear stress is parallel to the leading edge of the crevasse. Two-dimensional crevasse propagation is discussed in Section 8.3.

To account for stress concentrations near the crevasse tip, the stress intensity factor is introduced. This factor can be estimated from the geometry of the fracture and the net longitudinal stress (for example, Sih, 1973; Broek, 1986; Gdoutos, 1993). For the Mode I geometry shown in Figure 8.2, the stress intensity factor is (Broek, 1986, pp. 10–11)

$$K_I = \beta \sigma_t \sqrt{\pi d}, \quad (8.8)$$

where  $\beta$  is a dimensionless factor that depends on the geometry (crevasse spacing, height-to-width ratio, etc.),  $d$  the depth of the crevasse, and  $\sigma_t$  the external or remote tensile (or compressive) stress. If the stress intensity factor is greater than a critical value,  $K_{Ic}$ , fracture growth will occur until the stress intensity factor becomes equal to or less than  $K_{Ic}$ . This critical value is called the fracture toughness and is independent of the crevasse geometry. A review of experiments conducted on ice to determine its fracture toughness is given by Schulson and Duval (2009), and these results suggest  $K_{Ic} \approx 0.1$  to  $0.4 \text{ MPa m}^{1/2}$ . For low-density snow and firn, the critical stress intensity factor is considerably smaller, estimated to fall in the range of  $0.05$  to  $2.0 \text{ kPa m}^{1/2}$  (Schulson and Duval, 2009).

In the LEFM approach, crevasse growth results from an externally applied tensile stress. This growth is impeded by the ice overburden pressure, which increases with depth. Thus, as the crevasse penetrates deeper, the compressive stress at the crevasse tip becomes greater, effectively lowering the stress intensity factor. When considering single-mode fracturing (as done here for Mode I), the stress intensity factor resulting from a combination of applied stresses can be obtained by addition



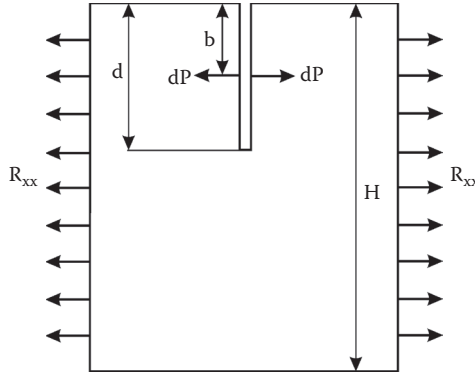


**FIGURE 8.3** Geometry and notation used for calculating the stress intensity factor for a single crevasse.  $dP$  represents the lithostatic force at depth  $b$  below the surface acting on a segment  $db$  of the crevasse wall. (Reprinted from Van der Veen, C. J., *Cold Regions Sci. Techn.*, 27, 31–47, 1998a. With permission from Elsevier.)

of stress intensity factors corresponding to each stress (Broek, 1986, p. 84). Thus, for crevasse propagation on glaciers, crevasse opening associated with a tensile stress and crevasse closure due to the lithostatic stress may first be considered separately; addition then gives the combined effect, allowing crevasse depth to be estimated. For a single crevasse, the geometry is shown in Figure 8.3.

Consider first opening of a single crevasse resulting from a tensile stress,  $R_{xx}$ , assumed to be constant throughout the ice thickness (depth variation can be included but makes the solution more complex). The corresponding stress intensity factor is (Broek, 1986, p. 85)

$$K_I^{(1)} = F(\lambda) R_{xx} \sqrt{\pi d}, \quad (8.9)$$

where

$$F(\lambda) = 1.12 - 0.23\lambda + 10.55\lambda^2 - 21.72\lambda^3 + 30.39\lambda^4, \quad (8.10)$$

with  $\lambda = d/H$  the ratio of crevasse depth to ice thickness. For shallow crevasses ( $\lambda \rightarrow 0$ ), this expression reduces to that used by Smith (1976, 1978),

$$K_I^{(1)} = 1.12 R_{xx} \sqrt{\pi d}. \quad (8.11)$$

Figure 8.4 shows the stress intensity factor as given by equation (8.9) as a function of crevasse depth, for different values of the ice thickness. The approximate solution (8.11), which assumes infinite ice thickness, is indistinguishable from the  $H = 2000$  m solution. For crevasses penetrating more than about 10% of the ice thickness, accounting for the finite thickness becomes important, and the stress intensity factor becomes greater than the approximate solution.



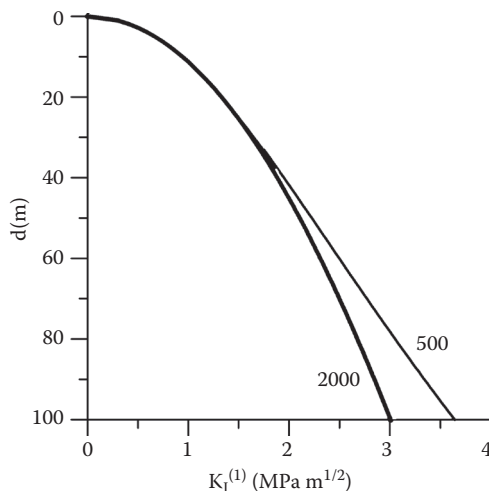


**FIGURE 8.4** Stress intensity factor at depth  $d$  below the surface for a tensile stress of 100 kPa, and ice thickness of 500 m and 2000 m.

The second process to consider is crevasse closure resulting from the compressive lithostatic stress. Because this stress cannot be considered constant, calculating the corresponding stress intensity factor is somewhat more involved than for the case of constant tensile stress. Following Rist and others (1996) and Van der Veen (1998a), the near-surface density profile is described by the following polynomial

$$\rho_f(h-z) = \rho - (\rho - \rho_s)e^{-C(h-z)}, \quad (8.12)$$

where  $\rho = 917 \text{ kg/m}^3$  represents the density of ice,  $\rho_s = 350 \text{ kg/m}^3$  the density of surface snow, and  $C = 0.02 \text{ m}^{-1}$ . The lithostatic stress at depth  $(h-z)$  below the surface is then

$$\begin{aligned} L(h-z) &= - \int_{h-z}^z \rho_f(\bar{z}) g d\bar{z} = \\ &= - \rho g(h-z) + \frac{\rho - \rho_s}{C} g (1 - e^{-C(h-z)}). \end{aligned} \quad (8.13)$$

To find the stress intensity factor associated with this lithostatic stress, the procedure of Hartranft and Sih (1973) is followed. Let  $b = h - z$  denote the depth below the surface. The lithostatic force acting over a small depth interval  $db$  is

$$dP(b) = L(b) db, \quad (8.14)$$

and the corresponding stress intensity factor is (Tada et al., 1973, p. 2.27)

$$dK_I^{(2)} = \frac{2L(b)db}{\sqrt{\pi d}} G(\gamma, \lambda). \quad (8.15)$$

The function  $G(\gamma, \lambda)$  is given by

$$G(\gamma, \lambda) = \frac{3.52(1 - \gamma)}{(1 - \lambda)^{3/2}} - \frac{4.35 - 5.28\gamma}{(1 - \lambda)^{1/2}} + \left[ \frac{1.30 - 0.30\gamma^{3/2}}{(1 - \gamma^2)^{1/2}} + 0.83 - 1.76\gamma \right] (1 - (1 - \gamma)\lambda), \quad (8.16)$$

where  $\gamma = b/d$  and  $\lambda = d/H$  as before.

The net stress intensity factor at the crevasse tip is found by integrating the contributions acting at different depths (equation (8.15))

$$K_I^{(2)} = \int_0^d dK_I^{(2)}. \quad (8.17)$$

Substituting equation (8.13) gives

$$K_I^{(2)} = \frac{2\rho g}{\sqrt{\pi d}} \int_0^d \left[ -b + \frac{\rho - \rho_s}{\rho C} (1 - e^{-Cb}) \right] G(\gamma, \lambda) db. \quad (8.18)$$

While an analytical expression for the integral is not readily obtained, the integral can be evaluated using standard numerical techniques. Note that the value of  $K_I^{(2)}$  is negative to indicate that this stress intensity factor is associated with the lithostatic stress tending to close a crevasse. Figure 8.5 shows the stress intensity factor calculated from equation (8.18) as a function of the crevasse depth,  $d$ , for a 2000 m thick glacier. Also shown is the constant density solution (light curve, obtained by setting  $\rho_s = \rho$  in equation (8.12)), which significantly overestimates the stress intensity factor.

Combining the two stress intensity factors given by equations (8.11) and (8.18) allows the penetration depth of a crevasse to be estimated. Figure 8.6 shows the net stress intensity factor for two values of the tensile stress. The vertical dashed lines indicate the lower and upper values of the estimated range for fracture toughness of glacial ice ( $0.1 - 0.4 \text{ MPa m}^{1/2}$ ; Schulson and Duval, 2009). Consider the curve corresponding to  $R_{xx} = 100 \text{ kPa}$ . Adopting the upper limit for the fracture toughness, in the upper 5 m the stress intensity factor is less than  $K_{Ic}$ , and crevasses shallower than 5.2 m cannot exist. However, if a crevasse has reached a depth of 5.2 m (for example, because it formed upstream under a greater tensile stress, or because it formed in low-density firn with a smaller fracture toughness), it has the potential

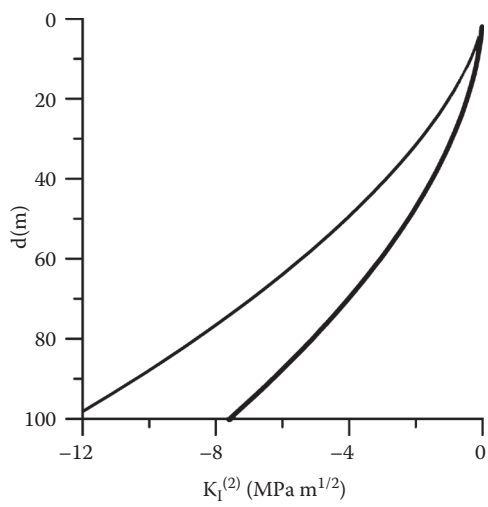


**FIGURE 8.5** Stress intensity factor at depth  $d$  below the surface corresponding to the lithostatic stress for 2000 m thick glacier. The heavy curve corresponds to the calculation including low-density firn at the surface, and the thin curve corresponds to the constant density solution.

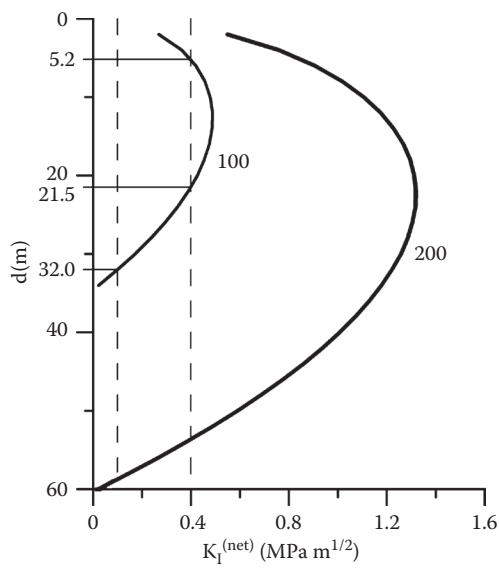


**FIGURE 8.6** Net stress intensity factor at depth  $d$  below the surface for two values of the stretching rate (100 kPa and 200 kPa). The dashed vertical lines correspond to the estimated lower and upper limits of fracture toughness of glacial ice.

to grow deeper because the stress intensity factor initially increases with depth. At some depth below the surface, the stress intensity factor reaches a maximum before decreasing with depth due to the effect of the lithostatic stress. For this example, the stress intensity factor becomes less than  $0.4 \text{ MPa m}^{1/2}$  at 21.5 m below the surface and further crevasse propagation is arrested. If the lower limit is adopted for the fracture toughness, the crevasse can penetrate to a depth of 32 m. Doubling the tensile stress to 200 kPa allows the crevasse to extend to a depth of 55–58 m, depending on the value for the fracture toughness.

Estimating crevasse depth using the LEFM approach is more involved than for the zero-stress model, and requires the stress intensity factor to be evaluated at depth for a range of model parameters to solve the expression

$$K_I^{(1)}(R_{xx}, d) + K_I^{(2)}(d) = K_{Ic}, \quad (8.19)$$

for the crevasse depth,  $d$ . Figure 8.7 shows crevasse depth as a function of the tensile stress for two values of the fracture toughness. Depending on whether a low or high value is adopted for  $K_{Ic}$ , a tensile stress of 30–80 kPa is required for crevasses to be able to exist. Also shown in Figure 8.7 is the crevasse depth derived by Weertman (1973b),

$$d = \frac{\pi}{2\rho g} R_{xx}. \quad (8.20)$$

This solution agrees with the constant-density LEFM solution, except for small values of the tensile stress. This difference arises because the Weertman solution (8.20)

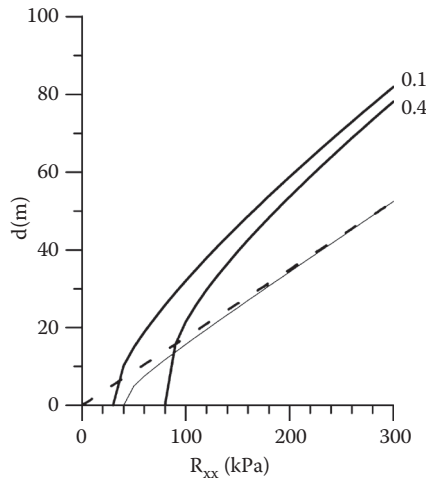


**FIGURE 8.7** Penetration depth of a water-free crevasse on a 2500 m thick glacier. Labels indicate the value of the fracture toughness used in  $\text{MPa m}^{1/2}$ . The dashed line represents the Weertman (1973) solution and the thin solid line the constant density solution. (Reprinted from Van der Veen, C. J., *Cold Regions Sci. Techn.*, 27, 31–47, 1998a. With permission from Elsevier.)

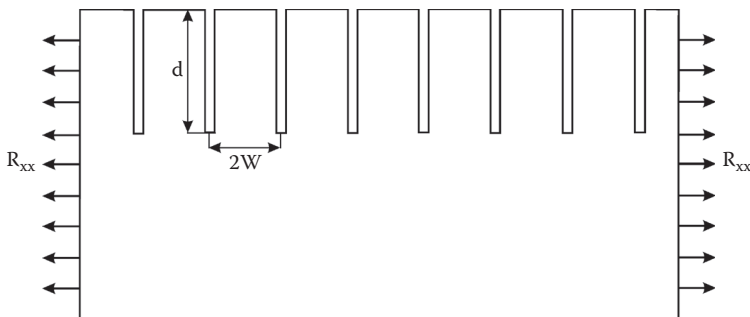


**FIGURE 8.8** Geometry and notation used for equally spaced crevasses under tension. The depth of all crevasses equals  $d$ , while the distance between neighboring crevasses equals  $2W$ . (Reprinted from Van der Veen, C. J., *Cold Regions Sci. Techn.*, 27, 31–47, 1998a. With permission from Elsevier.)

does not account for the strength of ice, and crevasses can exist for all values of the tensile stress. More importantly, assuming a constant density significantly underestimates the depth to which a crevasse can penetrate.

The discussion so far has focused on penetration depth of individual crevasses. Fields of closely spaced crevasses are probably more common on glaciers, and the “blunting” or “shadowing” effect will affect the stresses at the crevasse tips. In the thin slabs separating neighboring crevasses, no tensile stress exists, thus reducing stress concentrations (Weertman, 1973b). This only affects the stress intensity factor associated with the tensile stress; the lithostatic stress is the same for an individual crevasse and in a field of crevasses. For the geometry shown in Figure 8.8, the stress intensity factor is given by (Benthem and Koiter, 1973)

$$K_I^{(1)} = D(S)R_x \sqrt{\pi d S}, \quad (8.21)$$

where

$$D(S) = \frac{1}{\sqrt{\pi}} \left[ 1 + \frac{1}{2}S + \frac{3}{8}S^2 + \frac{5}{16}S^3 + \frac{35}{128}S^4 + \frac{63}{256}S^5 + \frac{231}{1024}S^6 \right] + 22.501S^7 - 63.502S^8 + 58.045S^9 - 17.577S^{10}, \quad (8.22)$$

and

$$S = \frac{W}{W + d}. \quad (8.23)$$

The assumption is made that the crevasses are evenly spaced at distance  $2W$  and that all crevasses have the same depth,  $d$ . This solution for the stress intensity factor applies to fractures in a semi-infinite half plane ( $d \ll H$ ).

For crevasses that are widely spaced ( $W \gg d$ ),  $S \approx 1$  and  $D(S) \approx 1.12$ , and the stress intensity factor equals the value estimated from equation (8.11) for an individual

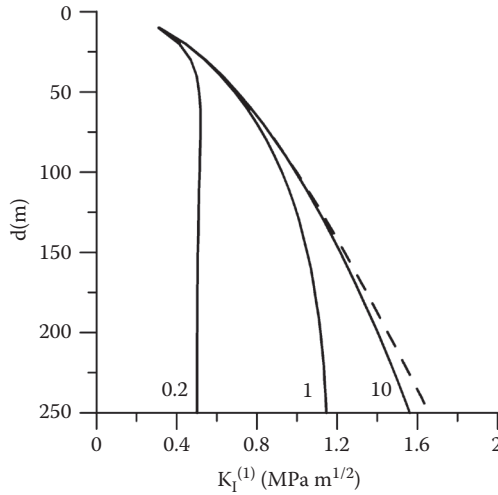


**FIGURE 8.9** Stress intensity factor associated with a tensile stress at depth  $d$  below the surface, for different values of crevasse spacing. Labels indicate crevasse spacing in km. The dashed line corresponds to the solution for a single crevasse.

crevasse. As crevasses become more closely spaced, the stress intensity factor decreases (Figure 8.9), and a larger tensile stress is needed for crevasses in a field to occur, in excess of 300 kPa for very closely spaced crevasses (Van der Veen, 1998a).

For tensile stresses typically found on glaciers and ice sheets, surface crevasses penetrate a few tens of meters downward, and their presence may be expected to have little effect on glacier flow and dynamics. That situation can change, however, when the crevasses become filled with surface meltwater. Because the density of water is greater than that of firn and ice, the pressure of water in the crevasse compensates part or all of the lithostatic stress, allowing the crevasse to penetrate deeper. This effect can be included by adding a stress intensity factor corresponding to the water pressure. The procedure is similar to that followed to arrive at equation (8.18) for the stress intensity factor associated with the lithostatic stress. The depth of the crevasse is denoted by  $d$ , and the water level in the crevasse is at a distance below the surface. At depth  $b > a$  the water pressure is

$$P_w(b) = \rho_w g(b - a), \quad (8.24)$$

where  $\rho_w$  represents the density of fresh water. Analogous to equation (8.18) the corresponding stress intensity factor is

$$K_I^{(3)} = \frac{2\rho_w g}{\sqrt{\pi d}} \int_a^d (b - a) G(\gamma, \lambda) db, \quad (8.25)$$

with  $G(\gamma, \lambda)$  given by equation (8.16).

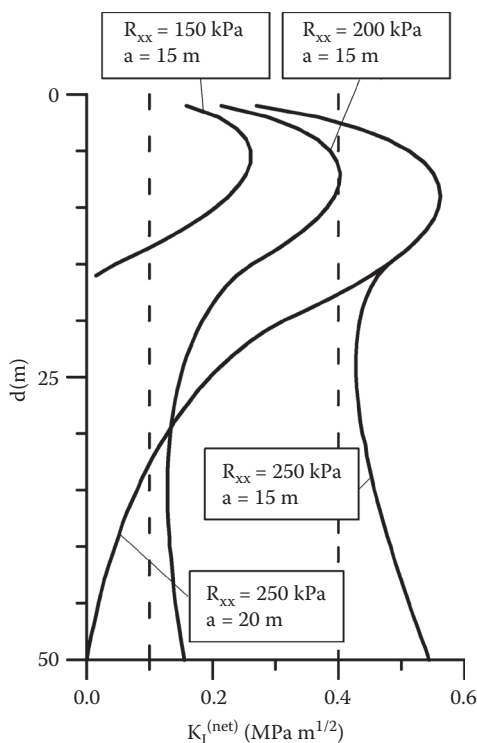


**FIGURE 8.10** Net stress intensity factor at depth  $d$  below the surface of any crevasse in a field of crevasses spaced at 500 m, for different combinations of model parameters. The vertical dashed lines represent the estimated lower and upper fracture toughness of glacier ice. (Reprinted from Van der Veen, C. J., *Cold Regions Sci. Techn.*, 27, 31–47, 1998a. With permission from Elsevier.)

The important parameter that determines whether water-filled crevasses can penetrate the full ice thickness is the depth of the water level below the surface,  $a$ , and, secondly, the tensile stress. Some net stress intensity factors for any crevasse in a field of crevasses spaced at 500 m are shown in Figure 8.10 for different combinations of model parameters. If the water level is sufficiently close to the surface ( $a \approx 10 \text{ m}$ ; Van der Veen, 1998a) and the tensile stress is greater than 100–150 kPa, a water-filled crevasse can reach the base of the glacier. This is the mechanism proposed by Van der Veen (2007) for how surface meltwater lakes can drain quickly and meltwater is transferred to the subglacial drainage system. In essence, hydrofracturing through the full thickness can occur provided the inflow of water into the crevasse is high enough to maintain a water level close to the surface. Generally, on cold glaciers, this will require abundant meltwater ponding on the glacier surface to initiate and sustain full thickness fracturing before refreezing at depth occurs. Das et al. (2008) report on rapid drainage (within less than two hours) of a supraglacial lake in West Greenland through 980 m of ice to the bed and argue that this drainage was initiated by water-driven fracturing that evolved into moulin drainage. Concurrent



ground-based measurements showed that drainage coincided with increased seismicity, a temporary increase in ice velocity and surface uplift, and followed by slowing down and subsidence over the next 24 hours.

The model described above is essentially one-dimensional, and only the vertical direction is considered. This is equivalent to making the assumption that crevasses extend infinitely into the transverse direction. Based on reported crevasse depths, which seldom exceed ~30 m (Holdsworth, 1968), compared with widths visible on the glacier surface, which are typically a few hundred meters to several kilometers, this assumption appears reasonable. However, the direct consequence is that the model cannot predict the crevasse orientation as seen on the surface in relation to the applied stress. To do so requires a two-dimensional model in which crevasse propagation in the transverse direction as well as in the vertical is considered. As shown in the next section, stress intensity factors can be calculated for elliptical cracks intersecting the surface, and these solutions can be used to evaluate crevasse propagation in the plane perpendicular to the longitudinal stress.

### 8.3 TWO-DIMENSIONAL CREVASSE PROPAGATION

The following discussion of map view propagation of crevasses is from Van der Veen (1999a) and applies to quasistatic crevasse propagation.

For an elliptical fracture in a uniform stress field, the stress intensity factor was determined by Newman and Raju (1981) using results of three-dimensional finite-element analysis. Referring to Figure 8.11 for the notation, and making the assumption that the fracture depth is small compared with the total thickness, the stress intensity factor is given by

$$K_I = \sigma \sqrt{\pi d} [1.13 - 0.09\lambda] [1 + 1.464\lambda^{1.65}]^{-1/2} [\lambda^2 \cos^2 \varphi + \sin^2 \varphi]^{1/4} [1 + 0.1(1 - \sin \varphi)^2], \quad (8.26)$$

with  $\lambda = d/w$  the ratio of fracture depth and half-length.

At  $\varphi = \pi/2$  (the deepest point of the fracture front), the stress intensity factor is

$$K_I(A) = \sigma \sqrt{\pi d} [1.13 - 0.09\lambda] [1 + 1.464\lambda^{1.65}]^{-1/2}, \quad (8.27)$$

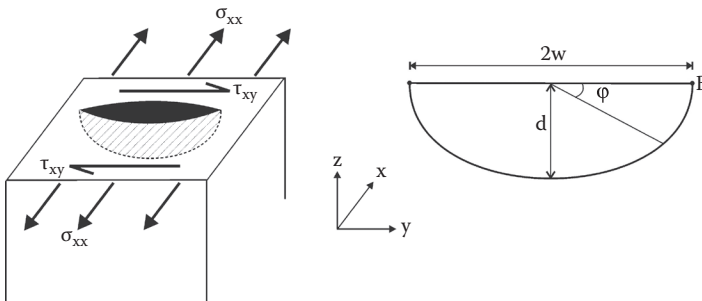


**FIGURE 8.11** Geometry of an elliptical surface crack. (Modified from Van der Veen, C. J., *Polar Geog.*, 23, 213–245, 1999a.)

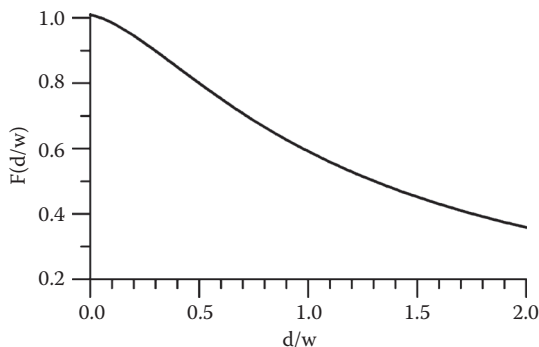


**FIGURE 8.12** Correction factor  $F(d/w)$  as a function of the depth-to-width ratio,  $d/w$ . (Modified from Van der Veen, C. J., *Polar Geog.*, 23, 213–245, 1999a.)

which can also be written as

$$K_I(A) = F(\lambda)K_I^{\text{edge}}, \quad (8.28)$$

where

$$K_I^{\text{edge}} = 1.12\sigma\sqrt{\pi d}, \quad (8.29)$$

represents the stress intensity factor for an edge fracture of depth  $d$  subject to a constant tensile stress,  $\sigma$  (Broek, 1986, p. 10). The function  $F(\lambda)$  is defined as

$$F(\lambda) = \frac{[1.13 - 0.09\lambda]}{1.12} [1 + 1.464\lambda^{1.65}]^{-1/2}, \quad (8.30)$$

and constitutes a correction factor to account for the two-dimensional structure of the elliptical fracture compared with the one-dimensional edge fracture. In Figure 8.12 this correction factor is shown as a function of the ratio  $\lambda = d/w$ . Crevasses on glaciers are usually much longer than they are deep and  $\lambda \rightarrow 0$  and  $F(\lambda) \approx 1$ . In other words, the depth of a crevasse on a glacier can, in good approximation, be estimated using the one-dimensional approach described in the previous section.

After the depth of the fracture is known, the length,  $2w$ , can be estimated by considering the stress intensity factor at the crevasse tips at the surface

$$K_I(B) = \sigma\sqrt{\pi d} [1.13 - 0.09\lambda] [1 + 1.464\lambda^{1.65}]^{-1/2} 1.1\sqrt{\lambda}, \quad (8.31)$$

or

$$K_I(B) = 1.1\lambda F(\lambda)K_I^{\text{plate}}, \quad (8.32)$$

with

$$K_I^{\text{plate}} = 1.12\sigma\sqrt{\pi w}, \quad (8.33)$$

the stress intensity factor of a through-the-thickness crack with length  $2w$ , in a plate subject to a tensile stress,  $\sigma$  (Broek, 1986, p. 10). Thus, the stress intensity factor at the surface equals that of a fracture penetrating the entire ice thickness multiplied by a correction factor to account for the partial penetration of the fracture. The length of the elliptical fracture can be estimated from the condition that the stress intensity factor at the tips (equation (8.32)) equals the fracture toughness.

Of interest here is the orientation of a crevasse as observed on the glacier surface. In a uniaxial stress field, the orientation of a fracture is perpendicular to the principal tensile stress, and fracture growth is in the plane of the original fracture such that, at the surface, the fracture remains straight. On glaciers, however, crevasses may be subject to combined loading of longitudinal tension and lateral shear. This fracturing can be described as a combination of Mode I (opening mode) and Mode II (sliding mode), and fracture propagation usually takes place at an angle with respect to the original fracture.

There are two approaches to estimating the propagation direction. According to the maximum principal stress criterion, fracture growth occurs in the direction perpendicular to the maximum principal stress at the fracture tip (Erdogan and Sih, 1963; Broek, 1986, p. 375). The strain energy density criterion postulates that a fracture propagates in the direction of minimum strain energy density (Sih, 1974; Broek, 1986, p. 377). Differences between orientations calculated from these methods are small (Broek, 1986, p. 380). Here, the maximum principal stress criterion is used because of its more clear physical meaning.

The stress intensity factor describes the stress distribution at the tip of a fracture. Because the problem is linear, stresses associated with Mode I and Mode II fracturing can be evaluated separately and added to yield the net stress. Consider first Mode I, in which the fracture opens in the direction of applied tensile stress. Denoting the corresponding stress intensity factor by  $K_I$  and using polar coordinates ( $r$ ,  $\theta$ ) (Figure 8.13), the stresses at the tip are (Broek, 1986, p. 96)

$$\sigma_{\theta}^{(I)} = \frac{K_I}{\sqrt{2\pi r}} \cos \frac{\theta}{2} \left[ 1 - \sin^2 \frac{\theta}{2} \right], \quad (8.34)$$

$$\tau_{r\theta}^{(I)} = \frac{K_I}{\sqrt{2\pi r}} \sin \frac{\theta}{2} \cos^2 \frac{\theta}{2}. \quad (8.35)$$

Similarly, the stresses associated with Mode II (resulting from shear in the plane of the fracture) are (Broek, 1986, p. 96)

$$\sigma_{\theta}^{(II)} = \frac{K_{II}}{\sqrt{2\pi r}} \left[ -\frac{3}{4} \sin \frac{\theta}{2} - \frac{3}{4} \sin \frac{3\theta}{2} \right], \quad (8.36)$$

$$\tau_{r\theta}^{(II)} = \frac{K_{II}}{\sqrt{2\pi r}} \left[ \frac{1}{4} \cos \frac{\theta}{2} + \frac{3}{4} \cos \frac{3\theta}{2} \right]. \quad (8.37)$$

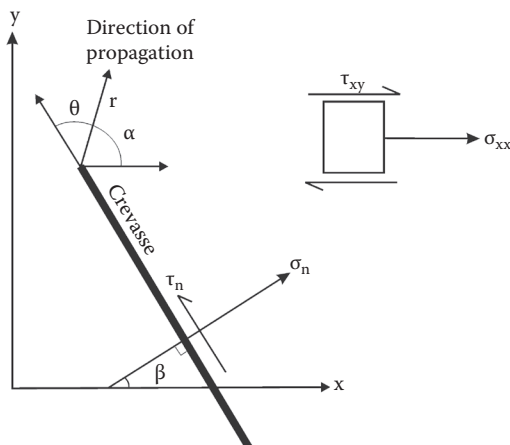


**FIGURE 8.13** Definition of angles used in deriving the direction of crevasse propagation. (Modified from Van der Veen, C. J., *Polar Geog.*, 23, 213–245, 1999a.)

Adding the two contributions gives the net stress at the tip of the fracture (Broek, 1986, p. 375)

$$\sigma_{\theta} = \frac{1}{\sqrt{2\pi r}} \cos \frac{\theta}{2} \left[ K_I \cos^2 \frac{\theta}{2} - \frac{3}{2} K_{II} \sin \theta \right], \quad (8.38)$$

$$\tau_{r\theta} = \frac{1}{2\sqrt{2\pi r}} \cos \frac{\theta}{2} [K_I \sin \theta + K_{II} (3 \cos \theta - 1)]. \quad (8.39)$$

It is now postulated that crevasse extension is in the direction for which  $\sigma_{\theta}$  is a principal stress or, equivalently, the direction for which  $\tau_{r\theta} = 0$ . This direction, represented by the angle  $\theta_m$ , is found by setting equation (8.39) to zero

$$K_I \sin \theta_m + K_{II} (3 \cos \theta_m - 1) = 0, \quad (8.40)$$

from which it follows that

$$\tan \frac{\theta_m}{2} = \frac{1}{4} \frac{K_I}{K_{II}} \pm \frac{1}{4} \sqrt{\left( \frac{K_I}{K_{II}} \right)^2 + 8}. \quad (8.41)$$

The direction of crevasse propagation,  $\theta_m$ , is defined with respect to the orientation of the crevasse, as illustrated in Figure 8.13. How the crevasse is oriented with respect to the external stresses, that is, with respect to a coordinate system fixed to the direction of glacier flow, determines the normal stress and shear stress acting on the crevasse, and hence the two stress intensity factors in equation (8.41).

Let  $\beta$  denote the angle between the crevasse orientation and the x-axis, the latter taken to be in the mean direction of ice flow. The tensile stress in the along-flow direction is  $\sigma_{xx}$  and the shear stress is  $\tau_{xy}$ . The stress acting perpendicular to the crevasse walls is then (Jaeger and Cook, 1976, p. 13)

$$\sigma_n = \sigma_{xx} \cos^2 \beta + 2\tau_{xy} \sin \beta \cos \beta, \quad (8.42)$$

while the shear stress parallel to the crevasse walls is given by

$$\tau_n = -\frac{1}{2}\sigma_{xx} \sin 2\beta + \tau_{xy} \cos 2\beta. \quad (8.43)$$

From these expressions, the two stress intensity factors at the tips of a crevasse of length  $2w$  can be estimated as

$$K_I = \sigma_n \sqrt{\pi w}, \quad (8.44)$$

$$K_{II} = \tau_n \sqrt{\pi w}. \quad (8.45)$$

The growth direction relative to the x-axis equals

$$\alpha = \frac{\pi}{2} + \beta - \theta_m, \quad (8.46)$$

and can be calculated as a function of the crevasse orientation using the formulas given above. However, as the crevasse propagates, the fracture orientation, and thus the angle  $\beta$ , changes. To account for this, the above expressions must be applied repeatedly to calculate the angle of propagation as the fracture grows in map view. In the case of only a far-field tensile stress,  $\sigma_{xx}$ , the orientation of the starter crack is unimportant. If the starter crack is misaligned from the tensile stress, the crevasse orients itself and the direction of growth is within a few degrees of the expected direction perpendicular to the tensile stress (Van der Veen, 1999a, Figure 10). For more complex stress configurations, crevasse propagation is not necessarily in the direction perpendicular to the principal tensile stress.

Consider the case of a tensile stress and a shear stress acting jointly on a crevasse. Such a stress configuration characterizes most valley glaciers and ice streams that are subject to lateral drag arising from friction between the moving ice and stagnant rock walls or more slowly moving interstream ridge ice. Making the assumption that crevasses form perpendicular to the principal tensile stress, the optimum angle,  $\beta_m$ , follows from the condition that the shear stress parallel to the crevasse walls,  $\tau_n$ , is zero, and

$$\tan 2\beta_m = \frac{2\tau_{xy}}{\sigma_{xx}}, \quad (8.47)$$

which is the expression derived earlier by William Hopkins (equation (8.2)). Figure 8.14 shows the crevasse orientation as a function of the stress ratio  $\tau_{xy}/\sigma_{xx}$  as predicted by the Hopkins model. For tension only, the crevasse is perpendicular to the direction of tensile stress, while in simple shear, the crevasse strikes at an angle

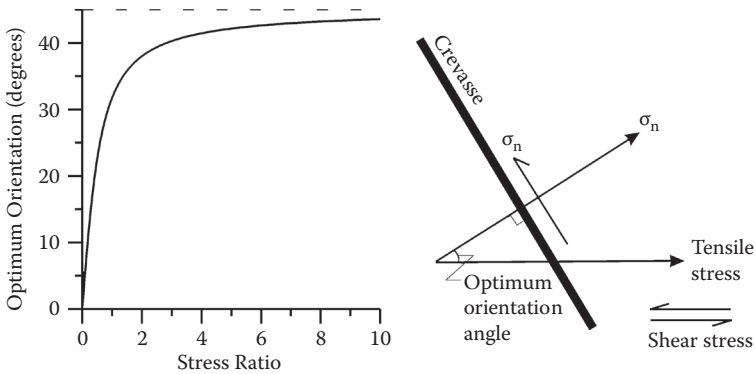


**FIGURE 8.14** Theoretically predicted orientation (defined with respect to the tensile axis) of a crevasse subject to tension and lateral shear, as a function of the ratio between shear stress and tensile stress. (Modified from Van der Veen, C. J., *Polar Geog.*, 23, 213–245, 1999a.)

of 45° to the x-axis. For the LEFM model, the direction of crevasse propagation can be evaluated as a function of the crevasse orientation. Results for different stress ratios are shown in Figure 8.15; the horizontal dashed lines correspond to the optimum direction calculated from equation (8.47).

In the LEFM approach, the reason that crevasse propagation is not necessarily in the direction perpendicular to the principal tensile stress is that combined Mode I and

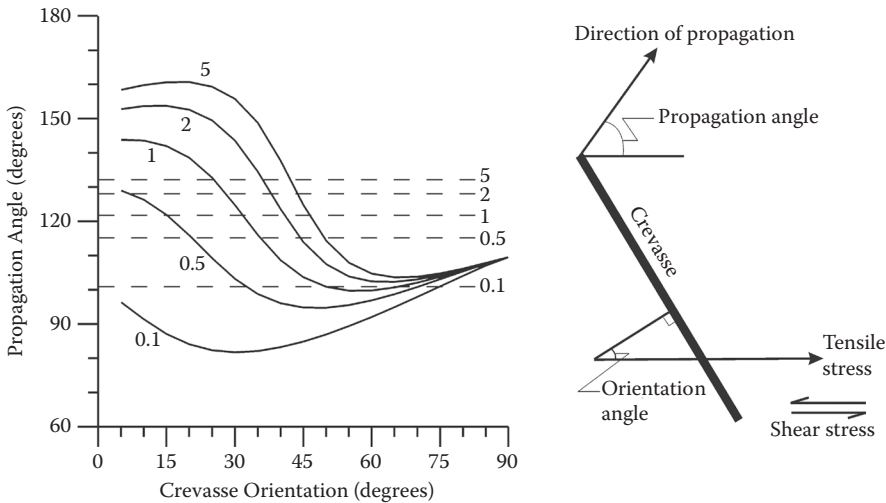


**FIGURE 8.15** Angle of propagation (defined with respect to the tensile axis) as a function of crevasse orientation, for different values of the ratio of shear stress and tensile stress (indicated by the labels). The horizontal dashed lines correspond to the direction of principal tensile stress. (Modified from Van der Veen, C. J., *Polar Geog.*, 23, 213–245, 1999a.)

Mode II fracturing is considered here. Mode I fracturing corresponds to the case of a fracture opening perpendicular to the (principal) tensile stress, while Mode II fracturing corresponds to strike-slip faulting, with the two faces of the fracture moving parallel to each other. If a crevasse were always to be perpendicular to the direction of principal tensile stress, fracturing would be described entirely by Mode I, as there would be no shear stress parallel to the crevasse walls. By allowing for strike-slip faulting (Mode II fracturing), this shear stress need not be zero, and consequently, the crevasse need not be oriented in the direction predicted by equation (8.47). This does not contradict the assumption that crevasse propagation is in the direction perpendicular to the principal tensile stress at the crevasse tip (equation (8.40)). Each fracturing mode leads to stress concentrations near the crevasse tip that are not simply scaled to the macroscopic stress field but, instead, are directionally dependent (equations (8.34)–(8.37)). Inspection of these equations shows that the direction of principal tensile stress at the crevasse tip is not necessarily the same as that of the macroscopic principal tensile stress.

In the discussion so far, no consideration has been given to the probability that a starter crack oriented at an angle  $\beta$  to the tensile axis develops into a mature crevasse. This point is investigated by considering the stress intensity factor at the crevasse tips.

For pure Mode I at fracture, the principal tensile stress at the tip of the fracture is

$$\sigma_1 = \frac{K_{Ic}}{\sqrt{2\pi r}}, \quad (8.48)$$

where  $K_{Ic}$  represents the fracture toughness of the material. For mixed-mode fracturing, it is postulated that crack extension takes place if the principal tensile stress at the crevasse tip has the same value as at fracture in an equivalent Mode I case (Broek, 1986, p. 376). That is,  $\sigma_\theta$  evaluated at  $\theta = \theta_m$  using equation (8.38) is set equal to  $\sigma_1$  from equation (8.48) to give

$$K_{Ic} = \cos \frac{\theta_m}{2} \left[ K_I \cos^2 \frac{\theta_m}{2} - \frac{3}{2} K_{II} \sin \frac{\theta_m}{2} \right], \quad (8.49)$$

or

$$K_{Ic} = K_I \cos^3 \frac{\theta_m}{2} - 3 K_{II} \cos^2 \frac{\theta_m}{2} \sin \frac{\theta_m}{2}. \quad (8.50)$$

The direction of propagation,  $\theta_m$ , as well as the two stress intensity factors,  $K_I$  and  $K_{II}$ , depend on the orientation of the crevasse through the angle  $\beta$ .

Figure 8.16 shows how the equivalent stress intensity factor varies as a function of crevasse orientation and ratio of shear stress to tensile stress. The equivalent stress intensity factor is normalized with the stress intensity factor for optimal crevasse orientation, that is, the direction for which the shear stress parallel to the crevasse walls vanishes (equation (8.47); these orientations are indicated by the vertical dashed lines). The curves in Figure 8.16 clearly show that the maximum equivalent stress intensity factor occurs for crevasse orientations that are different from the optimal



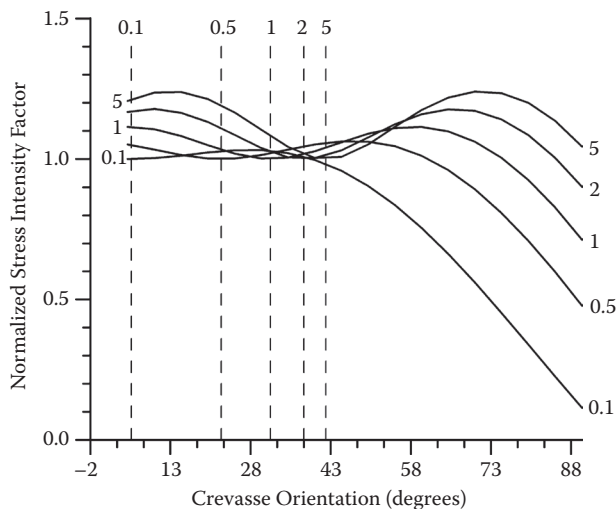


**FIGURE 8.16** Normalized equivalent stress intensity factor at the surface tips of an elliptical crevasse subject to tension and shear, as a function of crevasse orientation. Labels indicate the value of the ratio between lateral and tensile stress. Vertical dashed lines correspond to the optimal crevasse orientation with zero shear stress acting along the crevasse walls. (Modified from Van der Veen, C. J., *Polar Geog.*, 23, 213–245, 1999a.)

orientation perpendicular to the macroscopic principal tensile stress. The reason for this difference is that the Mode II stress intensity factor also contributes to the effective stress intensity factor, allowing this quantity to exceed the value calculated for Mode I fracturing only and used for normalization (equation (8.49)). This finding has important consequences for relating crevasse patterns to surface strain or stress. Fracture growth occurs when the (equivalent) stress intensity factor exceeds a threshold value, the fracture toughness of the material subject to fracturing. Now consider the curve labeled 2 in Figure 8.16, which shows two maxima where the effective stress intensity factor is about 1.2 times that corresponding to Mode I fracturing in the direction perpendicular to the principal tensile stress. Thus, initial cracks oriented at the corresponding angles are most likely to grow further, albeit in directions that are closer to the optimum orientation than the orientation of these starter cracks.

The model for crevasse initiation and propagation along the glacier surface discussed in this section (from Van der Veen, 1999a) assumes the glacier to be homogeneous and subject to a uniform stress field. Under those conditions, fractures will continue to propagate laterally. This is not very realistic; crevasses observed on glaciers have finite lengths, and propagation is often arrested at structural boundaries such as suture zones between ice originating from adjacent tributaries. This is clearly visible in the feature map of the Ronne Ice Shelf shown in Figure 8.17. This map was digitized by Hulbe and LeDoux (2011) from the MODIS (Moderate Resolution Imaging Spectroradiometer) Mosaic of Antarctica, a composite of images taken between November 20, 2003, and February 29, 2004, with a resolution of 125 m

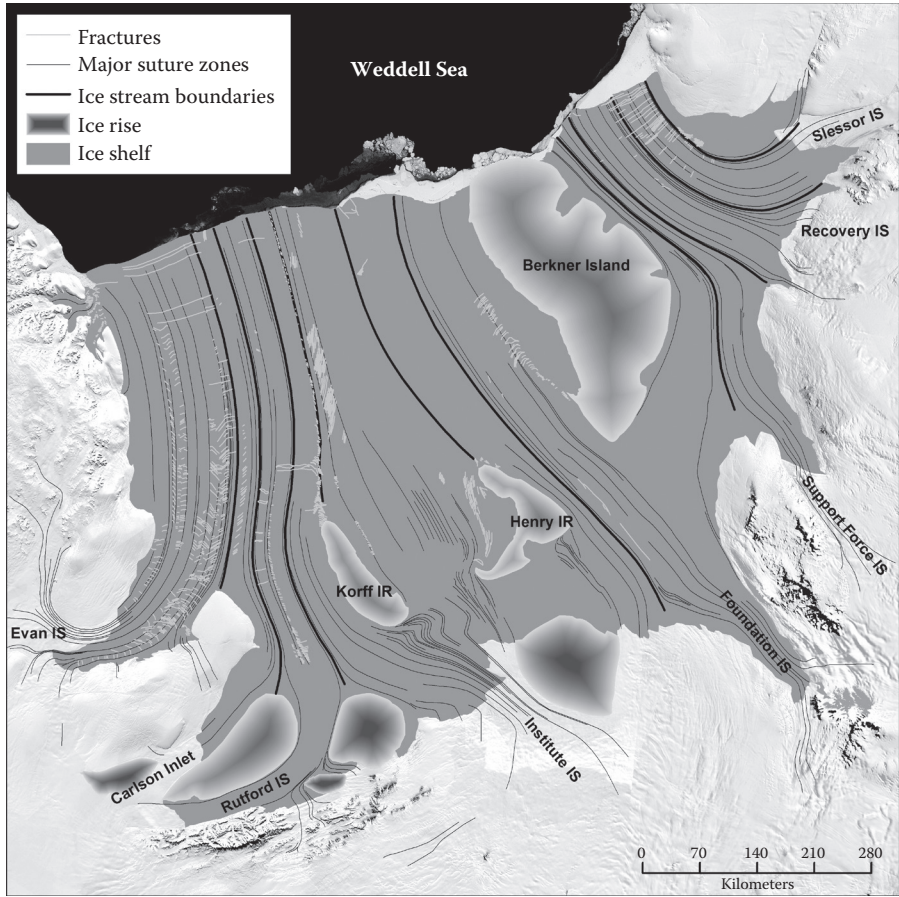


**FIGURE 8.17** Map showing surface features on the Ronne Ice Shelf digitized by Hulbe and LeDoux (2011) from the MODIS Mosaic of Antarctica shown as the background image. Major ice streams entering the ice shelf are shown, and their lateral margins can be traced across the ice shelf (dark lines). Light gray lines indicate sutures that appear to arrest lateral growth of crevasses. (Redrawn by Kyle Purdon using data files from Hulbe and LeDoux, 2011.)

(Scambos et al., 2007). A complete discussion of the features is given by Hulbe et al. (2010), but in short, it shows how fractures along the lateral boundaries of outlet streams feeding in the ice shelf are advected downstream and form long rifts. As the crevasses advect through the ice shelf, they propagate laterally with orientations dictated by the stress field. Over most of the ice shelf, the length of these fractures is constrained with locations of crack tip arrest coinciding with suture zones and other structural boundaries. Hulbe et al. (2010) use the displacement discontinuity boundary element method to model horizontal propagation of crevasses subject to Mode I and Mode II fracturing and show that, in the absence of suture zones, fractures would continue to propagate laterally. Thus, observed crevasse patterns indicate that growth is arrested by the presence of these suture zones.

A more heuristic approach to modeling fracture fields is adopted by Albrecht and Levermann (2012). Defining the two-dimensional fracture density field,  $\phi$ , as the mean area density of fractured ice with  $\phi = 0$  corresponding to crevasse-free regions, the assumption is made that the field is horizontally advected with the ice velocity,  $U$ . For one-dimensional flow along a central flowline, this gives

$$\frac{\partial \phi}{\partial t} + U \frac{\partial \phi}{\partial x} = f_s + f_h, \quad (8.51)$$

where  $f_s$  represents a local production term and  $f_h$  the rate at which crevasses are closing. Albrecht and Levermann (2012) make the assumption that the production term depends on the stretching rate and fracture density as

$$f_s = \gamma \dot{\epsilon}_{xx} (1 - \phi), \quad (8.52)$$

with  $\gamma$  a dimensionless parameter. The term in parenthesis reduces the local production proportional to crevasse density and reflects interactions among existing crevasses that tend to reduce the local stress.

Ignoring the healing term,  $f_h$ , the steady-state crevasse density is found by substituting equation (8.52) in the right-hand side of the advection equation (8.51) and setting the time derivative to zero. After some rearranging this gives

$$\frac{1}{1 - \phi} \frac{\partial \phi}{\partial x} = - \frac{\gamma}{U} \frac{\partial U}{\partial x}, \quad (8.53)$$

which can be integrated to give

$$\phi = 1 - (CU)^{-\gamma}. \quad (8.54)$$

The integration constant,  $C$ , can be found from the boundary condition that at the start of the flowline ( $x = 0$ ) the velocity equals  $U_o$  and the fracture density equals  $\phi_o$ . This yields the following solution for  $\phi$ :

$$\phi(x) = 1 - (1 - \phi_o) \left( \frac{U(x)}{U_o} \right)^{-\gamma}. \quad (8.55)$$

Albrecht and Levermann (2012) first apply their model to an idealized ice-shelf geometry. For an ice shelf that is sufficiently wide that lateral drag and lateral spreading may be ignored, the steady-state profiles derived in Section 5.5 can be used to find an analytical expression for  $\phi(x)$ . To keep the algebra simple, consider the profile corresponding to zero net mass balance (equation (5.71)). The corresponding velocity profile is

$$U(x) = H_o U_o \left[ \frac{(n+1)C}{H_o U_o} x + H_o^{-(n+1)} \right]^{-1/(n+1)}, \quad (8.56)$$

with

$$C = \left( \frac{\rho g (\rho_w - \rho)}{4 B \rho_w} \right)^n, \quad (8.57)$$

where  $\rho$  and  $\rho_w$  represent the density of ice and sea water, respectively, and  $B$  the viscosity parameter. Taking  $n = 3$ , the fracture density is then given by

$$\phi(x) = 1 - (1 - \phi_o) \left( \frac{4 C H_o^3}{U_o} x + 1 \right)^{-\gamma/4}. \quad (8.58)$$

This steady-state solution is shown in Figure 8.18 calculated using the following parameter values:  $\gamma = 0.5$ ,  $C = 7.73 \times 10^{-11} \text{ m}^{-3} \text{ yr}^{-1}$ ,  $\phi_o = 0.1$ ,  $H_o = 600 \text{ m}$ , and  $U_o = 300 \text{ m/yr}$  (Albrecht and Levermann, 2012). The fracture density increases rapidly just beyond the grounding line, where the stretching rate is largest and  $\phi$  relatively small. As  $\dot{\epsilon}_{xx}$  decreases and  $\phi$  increases, the local production rate decreases and the fracture density becomes almost constant.

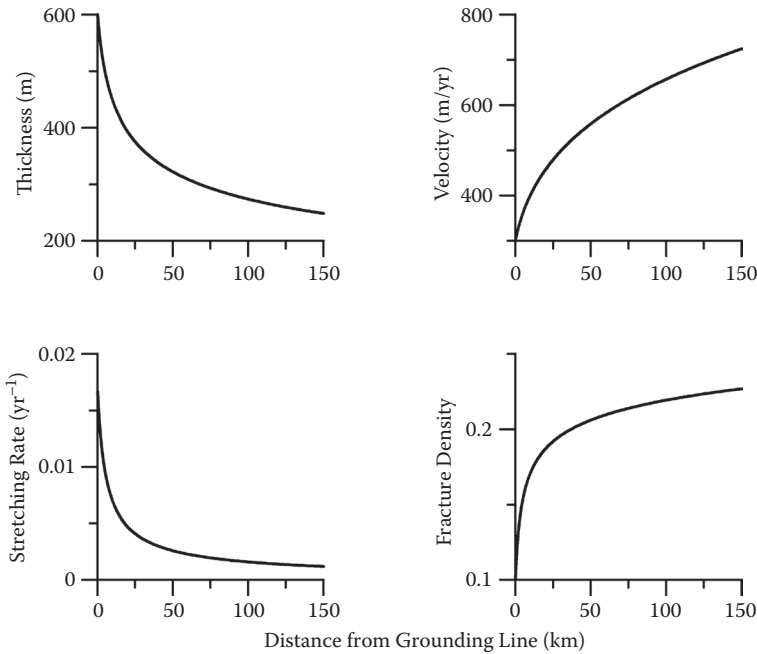


**FIGURE 8.18** Modeled fracture density on a free-floating ice shelf. The upper left panel shows ice thickness (equation (5.71)) and the upper right panel the velocity (equation (8.56)). The lower panels show the stretching rate on the left and fracture density (equation (8.58)) on the right.

For more realistic ice-shelf geometries, Albrecht and Levermann (2012) combine the fracture propagation model with a map-view numerical ice-shelf model solving for the stress balance using the shallow-shelf approximation. With appropriate choice of model parameters, simulated fracture density agrees qualitatively with observed fracturing on the Ronne–Filchner Ice Shelf (shown in Figure 8.17). As noted by the authors, the heuristic fracture model may provide an avenue to incorporate a more realistic calving boundary condition into map view models of ice shelves and floating ice tongues.

## 8.4 BASAL CREVASSES

Basal or bottom crevasses extend from the base upward into the ice. Their existence was suggested by Weertman (1973b) based on the analogy with a water-filled surface crevasse. Because bottom crevasses on floating glaciers are filled with sea water, the water pressure in the crevasse partially counters the weight-induced lithostatic stress, tending to close the crevasse. Using radar sounding, bottom crevasses have been detected on several ice shelves and floating ice tongues including the Ross Ice Shelf (Jezek et al., 1979; Anandakrishnan et al., 2007) and the Larsen Ice Shelf (Swithinbank, 1977; McGrath et al., 2012), as well as on grounded glaciers (for example, Harper et al., 2010).

For a free-floating ice shelf spreading in the  $x$ -direction only, the resistive stress,  $R_{xx}$ , is proportional to the ice thickness (equation (4.58)). For that case, Weertman (1973b, 1980) derived the following expression for the height of a basal crevasse

$$h = \frac{\pi H}{4}, \quad (8.59)$$

where  $H$  is the ice thickness. This crevasse height is greater than the height at which the net longitudinal stress is zero by a factor  $\pi/2$  as a result of stress concentrations at the crevasse tip. Where multiple closely spaced basal crevasses occur, these stress concentrations may be neglected (as in the case of fields of surface crevasses; Weertman, 1973b), and the crevasse height equals half the ice thickness. Jezek (1984) investigated height of basal crevasses on the Ross Ice Shelf and found that measured crevasse heights are considerably less than predicted by equation (8.59), indicating that the spreading stress is reduced compared with that for a free-floating ice shelf as a result of a compressive back stress.

A model for basal crevasses based on the LEFM approach is presented by Van der Veen (1998b), who investigated the conditions under which basal crevasses can occur. The model is very similar to that described in Section 8.2 for surface crevasses and is summarized in this section. The geometry is shown in Figure 8.19. A glacier of thickness  $H$  is considered, with  $z = 0$  at sea level, the ice surface at  $z = h$ , and the base of the glacier at  $z = b$  (negative if below sea level). The crevasse height above the ice base is  $d_b$ . As in the case of surface crevasses, three stresses contribute to the net longitudinal stress at depth, namely, the lithostatic stress (tending to close the crevasse), the water pressure in the bottom crevasse, and the tensile resistive stress,  $R_{xx}$ , both of which tend to open the crevasse.

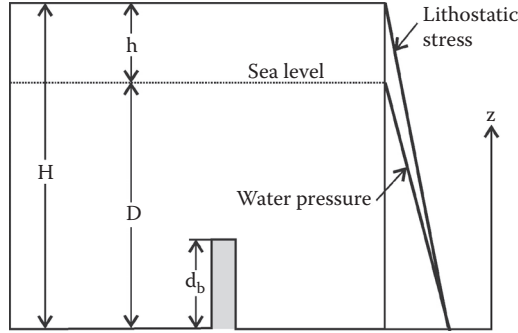


**FIGURE 8.19** Geometry used to calculate the penetration height of basal crevasses. (Reprinted from Van der Veen, C. J., *Cold Regions Sci. Techn.*, 27, 213–223, 1998b. With permission from Elsevier.)

Consider first the lithostatic stress. As in Section 8.2, allowance is made for the presence of low-density firn at the surface by adopting the density profile (8.12), and the lithostatic stress at depth is given by equation (8.13).

To estimate the opening stress associated with water filling the basal crevasse, the water pressure at the base of the glacier must be known. As shown in Section 7.4, this pressure must fall in the range

$$-\rho_w g b \leq P_w(b) \leq \bar{\rho} g H. \quad (8.60)$$

In this expression,  $\bar{\rho}$  represents the depth-averaged density. Note that for a floating ice shelf, the minimum and maximum water pressures are equal. Following Van der Veen (1998b), the water pressure at the bed is expressed in terms of the piezometric height,  $H_p$ , which equals the height above the base to which water in a borehole to the bed will rise. That is,

$$P_w(b) = \rho_w g H_p. \quad (8.61)$$

Introducing the height above buoyancy (or thickness in excess of flotation)

$$H_{ab} = H + \frac{\rho_w}{\bar{\rho}} b, \quad (8.62)$$

the inequality (8.60) can be rewritten as

$$0 \leq H_p + b \leq \frac{\bar{\rho}}{\rho_w} H_{ab}. \quad (8.63)$$

The water pressure in the crevasse is then given by

$$P_w(z) = \rho_w g (b + H_p - z), \quad (8.64)$$

at depths below the piezometric surface, and  $P_w(z) = 0$  above that surface.

The third stress to be considered is the tensile stress associated with glacier flow. In first approximation, this stress may be linked to the stretching rate as (compare with equation (4.62))

$$R_{xx}(z) = 2B(T)\dot{\epsilon}_{xx}^{1/3}, \quad (8.65)$$

where  $B(T)$  is the temperature-dependent viscosity parameter (equation (2.15)) and  $n = 3$  in the flow law. The assumption is made that the stretching rate,  $\dot{\epsilon}_{xx}$ , is constant with depth, and depth variation in the stretching stress is solely due to temperature variations. Van der Veen (1998b) adopts a simple linear temperature profile,

$$T(z) = \frac{h-z}{H}T_b + T_s, \quad (8.66)$$

where  $T_s$  and  $T_b$  represent the ice temperature at the surface and bed, respectively. Note that basal crevassing requires the presence of pressurized water at the glacier base so that the basal temperature equals the pressure melting temperature. In their application to the Larsen C Ice Shelf, McGrath and others (2012) adopt a parabolic temperature profile to estimate the tensile stress from measured surface strain rates.

In Section 8.2 stress intensity factors corresponding to each of the three stresses controlling crevasse propagation were estimated separately. This was done to discuss and illustrate how each stress contributes to the combined stress intensity factor. However, the combined stress intensity factor,  $K_I^{(b)}$ , can be found directly by integrating the net stress acting on the crevasse walls over the height of the crevasse, similar as the procedure leading to equation (8.18). Adding the three stress contributions, the net longitudinal stress at depth is given by

$$\sigma_n(z) = -\rho g(h-z) + \frac{\rho - \rho_s}{C} g [1 - e^{-C(h-z)}] + \rho_w g(H_p + b - z) + R_{xx}(z). \quad (8.67)$$

For a single basal crevasse, the net stress intensity factor is found by (numerical) integration

$$K_I = \int_b^{b+d_b} \frac{2\sigma_n(z)}{\sqrt{\pi d_b}} G(\gamma, \lambda) dz, \quad (8.68)$$

with the function  $G(\gamma, \lambda)$  given by expression (8.16) (Hartranft and Sih, 1973).

Consider first a single bottom crevasse on a floating ice shelf on which the height above flotation is zero and the piezometric height corresponds to sea level. In that case, there are three model parameters that determine the penetration height, namely, ice thickness, stretching rate, and surface temperature. Of these, the ice thickness has the smallest effect, with crevasse height decreasing by a few meters only for an increase in thickness from 500 to 2000 m (Van der Veen, 1998b, Figure 6). The other two parameters have a much stronger effect, as shown in [Figures 8.20](#) and [8.21](#).



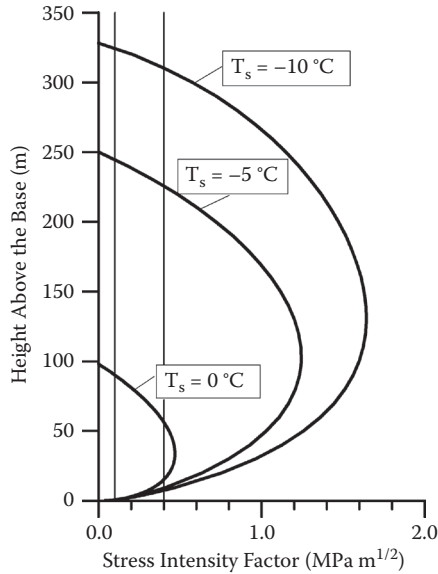


**FIGURE 8.20** Effect of surface temperature on the stress intensity factor for a floating ice shelf ( $H = 500$  m) and depth-independent stretching rate ( $\dot{\epsilon}_{xx} = 0.01 \text{ yr}^{-1}$ ). (Reprinted from Van der Veen, C. J., *Cold Regions Sci. Techn.*, 27, 213–223, 1998b. With permission from Elsevier.)

It may also be noted that accounting for the low-firn density layer through the density profile (8.12) has only a minor effect on the calculated stress intensity factor. This is because the density varies only near the surface (and thus affects penetration depth of surface crevasses), but for the lower parts of the glacier and over the height of bottom crevasses, the density is nearly constant.

Figure 8.20 shows the calculated stress intensity factor for three temperature profiles. In all three cases, the bottom temperature is set at  $0^\circ\text{C}$ . Close to the glacier base, the lithostatic stress and the water pressure nearly balance (at the base they are the same), and crevasse propagation is determined by the stretching stress,  $R_{xx}$  and, in first approximation, the stress intensity factor increases as the square root of crevasse height. Thus, as the crevasse grows, the stress intensity factor increases, allowing the crevasse to penetrate further. But as the crevasse extends farther into the ice, the water pressure decreases more rapidly than does the lithostatic stress, as schematically indicated in Figure 8.19. This causes the net longitudinal stress to decrease, and after reaching a maximum, which depends on the magnitude of the stretching stress, the stress intensity factor starts to decrease as the crevasse grows upward. The two vertical lines correspond to the lower and upper values for the fracture toughness of glacier ice given by Rist and others (1996), and crevasse height is given by the intersection of these lines with the curves of the stress intensity factor. While there are two solutions, the solution corresponding to a shallow crevasse is unstable and a small perturbation will cause the crevasse to either heal or grow to

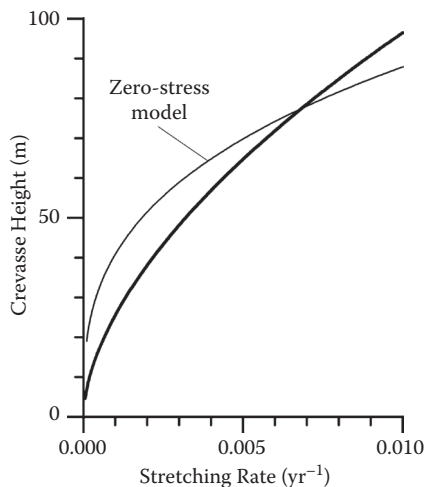


**FIGURE 8.21** Height of a bottom crevasse on an isothermal floating ice shelf ( $H = 500$  m;  $T_s = 0^\circ\text{C}$ ) as a function of stretching rate, using  $K_{Ic} = 0.1$  MPa m<sup>1/2</sup> for the fracture toughness. The thin curve represents the zero-stress solution. (Reprinted from Van der Veen, C. J., *Cold Regions Sci. Techn.*, 27, 213–223, 1998b. With permission from Elsevier.)

the second, stable solution. As shown, the colder the surface ice, the higher a basal crevasse will penetrate upward. This is because, for constant stretching rate, the corresponding stress increases as the temperature decreases. Similarly, increasing the stretching rate allows the crevasse to penetrate farther into the ice (Figure 8.21). For the isothermal case shown in this figure, the crevasse height estimated from the zero-stress model in which the crevasse grows upward to the level where the net longitudinal stress is zero agrees well with the full solution.

McGrath and others (2012) identified a series of basal crevasses along a 31 km long transect across the northern sector of the Larsen C Ice Shelf in the Antarctic Peninsula. These crevasses show as clear refractions in echograms obtained from ground-penetrating radar. Near the lower end of the transect, individual crevasses penetrating 70–134 m into the ice and that are widely spaced (0.5–2.0 km) are observed. The crevasse opening width (at the base of the ice shelf) ranges from 20–70 m at the upstream end to 150–240 m on the last 15 km of the transect. Apparently, the more widely spaced crevasses transitioned from a region of multiple shallow basal fractures. Applying a model similar to that described in this section and using measured surface strain rates to estimate the stretching stress, these authors find that the LEFM model accurately predicts the height to which the basal crevasses penetrate. As would be expected for floating ice, surface troughs observed in visible imagery overlie the major basal crevasses. These surface depressions are likely to result in ponding of surface meltwater, which would create the reservoir needed for meltwater-driven hydrofracturing (Section 8.2) and, because these depression exist in conjunction with basal crevasses, could promote full-thickness fracturing (McGrath et al., 2012; c.f. Section 8.5).

For grounded glaciers, the most important parameter that determines whether basal crevasses can occur is the height of the piezometric head above the glacier base, which in turn depends on the basal water pressure. Rather than discussing the results in terms of height above buoyancy, the concept of flotation level is used here. This level is defined as

$$H_f = \frac{\bar{\rho}}{\rho_w} H, \quad (8.69)$$

and the difference between the piezometric head and this level is used to estimate crevasse propagation. This difference,  $\Delta H_p = H_f - H_p$ , describes how close the grounded glacier effectively is to flotation, irrespective of the height above buoyancy; where this difference is zero, the basal water pressure equals the ice overburden pressure and the effective pressure at the bed is zero. Note that because meltwater under glaciers is fresh, the density for fresh water should be used in these expressions.

The contour map in Figure 8.22 shows how the crevasse height depends on stretching rate and depth of the piezometric head below the flotation level. Even a small drop of a few meters below the flotation level can inhibit the growth of basal crevasses. Thus, basal crevasses can only occur where the basal water pressure is close to the ice overburden pressure and the glacier is effectively near flotation.

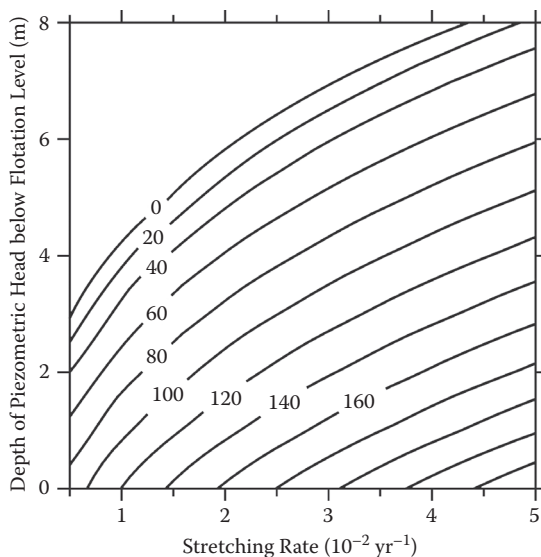


**FIGURE 8.22** Contour map of basal crevasse height on a grounded glacier as a function of the depth of the piezometric head below the flotation level and stretching rate ( $T_s = 0^\circ\text{C}$ ). (Reprinted from Van der Veen, C. J., *Cold Regions Sci. Techn.*, 27, 213–223, 1998b. With permission from Elsevier.)

## 8.5 ICEBERG CALVING

Calving occurs where a floating or grounded glacier terminus meets the ocean or a proglacial lake, and blocks of ice detach from the glacier to form icebergs ranging in size from small bits and pieces to large tabular icebergs. It is the only mechanism by which ice is rapidly transferred from grounded glaciers and ice sheets to the world's oceans. Calving into proglacial lakes and embayments has been implicated as the process responsible for the rapid disappearance of large Northern Hemisphere ice sheets following the last glacial maximum (for example, Pollard, 1984; Stokes and Clark, 2004), with recurrent episodes of armadas of icebergs invading the North Atlantic (Heinrich Events) documented in ocean sediment cores (Heinrich, 1988; Bond and Lotti, 1995). More recently, retreat of floating calving termini in Greenland and Antarctica occurred concurrently, with large changes in discharge from the grounded feeder glaciers (for example, De Angelis and Skvarca, 2003; Joughin et al., 2004) and have raised concerns about accelerated contributions from the polar ice sheets to global sea level rise as climate continues to warm. At the present, iceberg calving accounts for almost all of the mass loss of the Antarctic Ice Sheet (Rignot et al., 2008) and perhaps as much as half the mass loss of the Greenland Ice Sheet (Van den Broeke et al., 2009). Yet the controls on calving rate or terminus position remain the topic of debate.

A wide range of calving environments exists, producing icebergs the size of small bergy bits to large tabular icebergs detaching from floating Antarctic ice shelves. As a start, two main factors can be identified as determining the type of calving, namely, whether the glacier is cold or temperate, and whether the terminus is grounded or floating. This gives four possible calving termini, of which three are known to exist. Temperate glaciers usually do not form floating ice tongues, although the terminus of Columbia Glacier in Alaska became ungrounded in 2007 as the glacier continued its prolonged retreat (Walter et al., 2010). Within the warm, grounded category a further distinction can be made between glaciers terminating in freshwater lakes and those terminating in sea water. To differentiate between these types of calving, the term *tidewater calving* is applied to calving from termini grounded in sea water, while the term *lacustrine calving* refers to calving from grounded glaciers that terminate in freshwater proglacial lakes. For comparable geometries—in particular water depth—calving rates on lacustrine glaciers are an order of magnitude smaller than those on tidewater glaciers (Funk and Röthlisberger, 1989; Warren et al., 1995; Warren and Aniya, 1999).

The type of iceberg produced by calving glaciers depends on the type of glacier terminus. Tidewater glaciers usually produce icebergs that are relatively small compared with the size of the glaciers, with dimensions of a few hundred meters at most. The rate at which these smaller bergs are produced can be large, in particular during rapid retreat, jamming the adjacent fjord waters with floating icebergs. Greenland tidal outlet glaciers usually produce larger bergs, with horizontal dimensions up to a few km. Calving from Antarctic ice shelves is more infrequent, with long periods of little or no calving activity punctuated by the detachment of large tabular icebergs that appear to originate as a result of giant rifts cutting through these ice shelves (Lazzara et al., 1999).

Given the range of calving environments and the essentially stochastic nature of iceberg detachment, one could question whether a deterministic universal calving relation exists. Calving involves propagation of fractures through the ice, which depends on the local stress regime, presence of pre-existing cracks (surface crevasses), strength of the ice, availability of surface meltwater, and other factors. Accounting for all these effects in a universally applicable calving relation may be an illusory quest. Nevertheless, it may be possible to formulate a “bulk calving relation” that can be implemented in numerical models and that reflects temporally averaged behavior of calving glaciers. That is, no attempt is made to model production of individual icebergs, but rather, an average rate of iceberg production is predicted. In this section, several models that have been proposed are reviewed.

Traditionally, most systematic calving observations derive from tidewater glaciers. A tidewater glacier is a glacier that terminates in the sea, where it usually ends in an ice cliff from which icebergs are discharged. In the polar regions, the terminus may be floating; but temperate tidewater glaciers, such as those found in Alaska, are usually grounded up to the calving ice front although parts of the terminal region may incidentally become afloat. Floating tidewater glaciers are essentially ice shelves that have formed in fjords or valleys.

The position of the terminus of tidewater glaciers appear to go through cycles of slow advance, typically at a rate of several tens of meters per year, lasting perhaps as long as 1000 yr, followed by much shorter periods of rapid retreat (Meier and Post, 1987). Typical retreat rates range from a few hundred meters per year to a few kilometers per year. The cyclic behavior of tidewater glaciers is illustrated in Figure 8.23, starting with the terminus at its most advanced position (panel a). The front of the

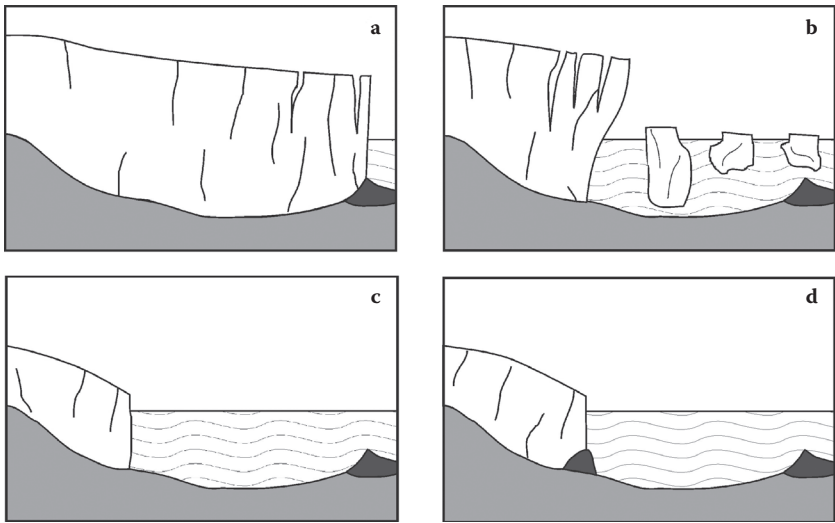


**FIGURE 8.23** Illustrating the life cycle of tidewater glaciers from the most advanced position (panel a) through rapid retreat (panel b) to the most retracted position (panel c), followed by slow advance of the glacier terminus (panel d).

glacier rests on a terminal moraine shoal at the end of the fjord. A large portion of the advanced glacier lies in the ablation area, where surface melting during the summer exceeds winter snowfall. This may render the terminus position more susceptible to small perturbations in climate or ablation rate. While the glacier front cannot readily advance, a moderate thinning could cause the terminus to retreat into deeper water, resulting in increased calving rates and accelerated retreat (panel b). Retreat of the terminus is halted where the water depth becomes sufficiently shallow to reduce the rate of iceberg production (panel c). Subglacial erosion and transport of sediment results in the formation of a new moraine at the foot of the retracted terminus position (panel d). This moraine reduces the water depth at the terminus, allowing the front to advance as the moraine is being recycled in a conveyor-belt fashion. The rate of advance is slow, determined mainly by how fast material is eroded from the upglacial side of the moraine and deposited on the seaward side. Advance is halted when the terminus reaches the end of the fjord or where the fjord widens.

There is no obvious climatic control on the change in terminus position. Rather, the behavior of a tidewater glacier may be largely controlled by the phase of the cycle and by the balance between calving rate and glacier speed. Neighboring glaciers are known to behave markedly differently. For example, Harvard and Yale Glaciers both terminate in College Fjord, which feeds into Prince William Sound, Alaska, and derive from the same snowfields as Columbia Glacier. Harvard Glacier has been advancing at a rate of about 20 m/yr since 1899, while its immediate neighbor, Yale Glacier, appears to have retreated since the early 19th century. Initially, this retreat was at a modest rate of about 7 to 11 m/yr, but since 1957, the rate of retreat has increased considerably, reaching 345 m/yr between 1974 and 1978. More recently, the retreat of Yale Glacier has slowed and the ice front may have reached its stable retracted position (Sturm et al., 1991). Despite these different behaviors of neighboring calving glaciers, there is some suggestion that the initiation of retreat may be associated with climate. During several decades prior to the onset of retreat, the net surface mass balance of Columbia Glacier was negative (Tangborn, 1997). This may have caused the terminal region to thin and become unstable, leading to the rapid retreat of the calving front. Perhaps prolonged periods of warmer-than-usual climate predispose a tidewater glacier in its most advanced position to collapse. Once initiated, however, the course of retreat appears to be largely controlled by internal dynamics rather than climate factors.

The scenario for slow advance followed by rapid retreat is based largely on the linear relation between water depth and calving rate derived by Brown et al. (1982), who conducted a statistical analysis of data for 12 Alaskan tidewater glaciers and found that the annual calving rate,  $U_c$  (in km/yr), is correlated with the water depth,  $D$  (in m), as

$$U_c = 0.024 D. \quad (8.70)$$

Similar relations have been found for other glaciers (for example, Pelto and Warren, 1991; Kennett et al., 1997), but a number of questions remain that cast doubt on the water-depth relation as a viable explanatory and predictive model for iceberg calving (Van der Veen, 1996, 2002a).

A first objection against the water-depth relation is that this model applies to annual-averaged calving rates only (Brown et al., 1982) and breaks down when seasonal calving rates are considered (Sikonia, 1982; Krimmel, 1997; Meier, 1997). Moreover, even if annual-mean calving rates are considered, the water-depth model does not explain all of the variations in calving rate observed on Columbia Glacier. From late 1984 to early 1989, the calving rate on this glacier remained more or less constant, yet the terminus continued to retreat into deeper water, with the water depth increasing from around 200 m to around 300 m. Since then, the calving rate doubled, despite the terminus remaining grounded at a water depth of around 350 m (Van der Veen, 2002a, Figure 6). Meier and Post (1987) propose that the linear calving relation may apply to glaciers whose terminus is close to steady state, but that another calving relation becomes important during the period of accelerated retreat of the terminus. These authors also point out that the terminus appears to retreat to the point where the effective basal pressure approaches zero.

A second observation that casts doubt on the water-depth model is that, during its rapid retreat, the speed of Columbia Glacier increased almost as much as did the calving rate, and an excellent correlation exists between these two quantities. A similar linear relation between glacier speed and calving rate exists for the other Alaskan glaciers considered by Brown et al. (1982), as well as for lacustrine calving glaciers and for 12 floating tidal glaciers in northern Greenland (Van der Veen, 2002a). If, indeed, the calving rate is determined by geometrical factors such as water depth at the terminus, there is no physical explanation why these factors would cooperate with physical processes affecting glacier speed that both would vary in unison on both grounded tidewater glaciers and floating ice tongues. It may be noted that on short time scales (on the order of days), the correlation between calving rate and ice speed breaks down. O'Neel et al. (2003) measured ice motion and terminus positions at 2 to 8 hour intervals nearly continuously between May 2 and June 4, 1999, on LeConte Glacier, Alaska. Over this 30-day period they found no significant variation in ice flux to the terminus, but large variations in the calving flux. As noted earlier, calving is a highly stochastic process and, as a result, the terminus position can fluctuate significantly over short time scales, for example, after a major calving event. These individual events need not directly correlate with ice velocity and are likely controlled by other factors such as tidal forcing, subaerial collapse of seracs, forward toppling of overhanging cliffs, notch melting at the water line, existing planes of structural weakness, and so forth. However, when averaged over time periods sufficiently long to reduce the importance of individual calving events (about 10 days or so; O'Neel et al., 2003, Figure 5), the calving flux appears to be mostly constant over the time period considered. The goal of any calving criterion discussed in this section is not to predict individual calving events, but rather, to predict the average calving rate or change in terminus position. Thus, the observations of O'Neel et al. (2003) do not necessarily negate the arguments presented by Van der Veen (1996, 2002a).

A different mechanism for iceberg calving is suggested by Van der Veen (1996), based on the observation that during the retreat of Columbia Glacier, the thickness at the terminus remained at about 50 m in excess of the flotation thickness. This



suggests that calving occurs whenever the terminal thickness in excess of flotation becomes less than some critical value, given by

$$H_c = \frac{\rho_w}{\rho} D + H_o, \quad (8.71)$$

where  $D$  represents water depth,  $\rho$  and  $\rho_w$  the densities of sea water and ice, respectively, and  $H_o$  the thickness at the terminus in excess of flotation ( $H_o \approx 50$  m for Columbia Glacier). Vieli et al. (2001) proposed a slightly modified relation where the minimum height above buoyancy is replaced by a small fraction,  $q$ , of the flotation thickness at the terminus and

$$H_c = \frac{\rho_w}{\rho} (1 + q) D. \quad (8.72)$$

The height-above-buoyancy model is essentially different from previous models because the *position* of the terminus is determined by the local water depth and ice thickness, whereas in earlier models, the *calving rate* is linked to these parameters. According to Van der Veen (1996), retreat is initiated when the thickness at the terminus becomes too small to maintain contact with the bed, and the rate of retreat is controlled by the thinning rate of the snout and by the ice speed. Consequently, if the glacier speed increases (as it did during the retreat of Columbia Glacier), the calving rate increases simultaneously to maintain the rate of terminus retreat. The implication of this scenario is that the rapid retreat of tidewater glaciers is not the result of increased calving as the glacier retreated into deeper water. Instead, retreat is initiated and maintained by thinning of the glacier, probably associated with an increase in ice discharge and perhaps the preceding period of negative net surface mass balance. Thus, retreat may be expected to continue as long as large ice speeds are maintained.

Vieli et al. (2001) incorporate the calving relation (8.72) into a numerical model simulating advance and retreat of a tidewater glacier. In their model, the calving rate is a derived quantity obtained from the difference between ice velocity at the terminus and change in terminus position. Interestingly, a linear relationship between calving rate and water depth is found for the case of a slowly advancing or retreating terminus, but not for rapid terminus changes. Rapid retreat or advance of the terminus is controlled by basal topography and occurs preferentially where the bed slopes upward in the downglacier direction. During retreat through a basal depression, the ice velocity near the terminus increases because the sliding velocity is taken inversely proportional to the effective basal pressure. Whether or not the terminus is able to advance across a bed overdeepening depends on the water depth and the fraction,  $q$ , in the calving criterion (8.71). If the maximum water depth is too great, readvance cannot occur because mass loss by calving remains too large. A similar result was obtained by Nick et al. (2007), who employed a similar flowline model to simulate advance and retreat of Columbia Glacier. That study implemented both the water-depth calving criterion (8.70) and the height-above-buoyancy criterion

(8.72) and found that both yielded similar glacier behavior. Once initiated, retreat is rapid and continues until shallower water depth at the head of the fjord is reached. Irrespective of accumulation rate and calving criteria, the terminus does not advance into deeper water ( $>300$  m water depth) unless sedimentation at the glacier front is included. By incorporating “conveyor belt” recycling of subglacial sediment and the formation of a sediment bank at the terminus, advance across basal troughs becomes possible, with the rate of advance determined by the rate of proglacial sediment deposition.

As noted by Benn et al. (2007a), a fundamental shortcoming of the height-above-buoyancy model is that it precludes the formation of ice shelves and floating ice tongues because the terminus position is always at a location where flotation has not been reached yet. This behavior contrasts with the observation that Columbia Glacier became ungrounded in 2007 (Walter et al., 2010). Further, many of the outlet glaciers in Greenland appear to form small floating ice tongues from which icebergs are discharged. To overcome this limitation of the calving criterion (8.71) or (8.72), Benn et al. (2007b) propose a criterion based on downward propagation of surface crevasses: calving occurs where the depth of surface crevasses equals the height above sea level or, equivalently, where the surface crevasse reaches water level. Nick et al. (2010) propose a modification of this calving model and posit that calving will occur where surface crevasses reach the depth to which basal crevasses penetrate upward into the ice (Figure 8.24).

In a field of closely spaced crevasses, there are no large stress concentrations near the tips of crevasses (Weertman, 1973b), and the penetration depth of surface crevasses may be estimated based on the assumption that crevasses will penetrate to the

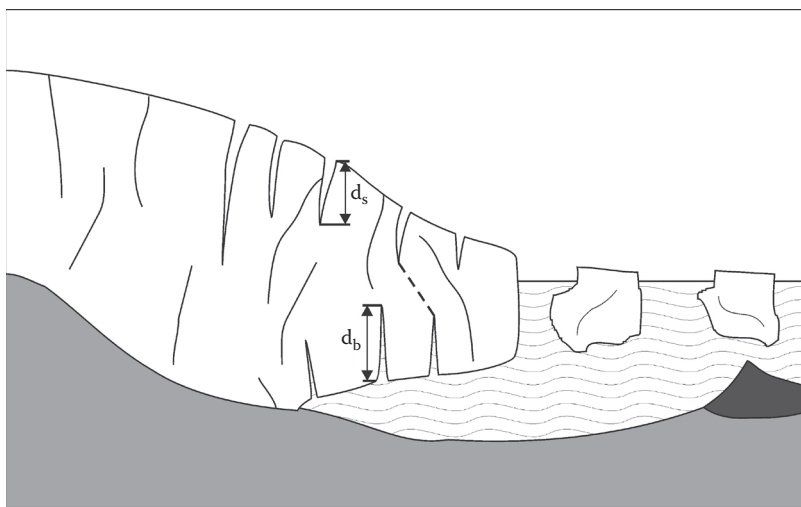


**FIGURE 8.24** Geometry used in the crevasse-penetration calving model. The dashed line connecting the surface and bottom crevasse represents the intact part of the ice thickness along which shear failure may occur.

depth at which the longitudinal stress equals the compressive overburden pressure (equation (8.7)). If the crevasse is partially filled with water, the additional opening stress associated with the weight of the water allows deeper penetration, and the crevasse depth is given by (Benn et al., 2007b)

$$d_s = \frac{R_{xx}}{\rho g} + \frac{\rho_{ws}}{\rho} d_w. \quad (8.73)$$

In this expression,  $\rho_{ws}$  represents the density of surface meltwater filling the crevasse and  $d_w$  the water height in the crevasse so that the water level is at a depth  $d_s - d_w$  below the ice surface.

Similarly, the propagation height of basal crevasses can be estimated from the condition that at this height, the net longitudinal stress must be zero. This stress is derived in Section 8.4 and given by equation (8.67). Ignoring the low-density firn layer (second term on the right-hand side) and assuming an easy connection between the subglacial drainage system and the adjacent ocean or lake (so that the piezometric height equals the depth,  $D$ , of the glacier base below sea or lake level), the net longitudinal stress is given by

$$\sigma_n(z) = -\rho g(h - z) + \rho_{wb} g(D - z) + R_{xx}. \quad (8.74)$$

The tensile stress,  $R_{xx}$  is taken constant throughout the ice thickness;  $\rho_{wb}$  denotes the density of sea water (tidewater calving) or fresh water (lacustrine calving). Setting  $\sigma_n(z)$  equal to zero yields

$$z = \frac{\rho}{\rho_{wb} - \rho} \left[ h - \frac{\rho_{wb}}{\rho} D + \frac{R_{xx}}{\rho g} \right]. \quad (8.75)$$

After some rearranging, the penetration height is found to be

$$d_b = \frac{\rho}{\rho_{wb} - \rho} \left( \frac{R_{xx}}{\rho g} - H_{ab} \right), \quad (8.76)$$

where  $H_{ab}$  represents the height above buoyancy, defined as

$$H_{ab} = H - \frac{\rho_{wb}}{\rho} D. \quad (8.77)$$

Nick et al. (2010) present results from the numerical flow-band model described in Section 9.4 and compared two calving criteria based on crevasse propagation. Model behavior is very similar, whether the position of the calving front is defined as the location where surface crevasses reach the waterline or whether this position is where surface and basal crevasses penetrate the full ice thickness. More important is the markedly different glacier behavior as compared to earlier studies in which calving is included through the water-depth relation or height-above-buoyancy criterion. The latter two calving models do not allow a floating ice tongue to develop

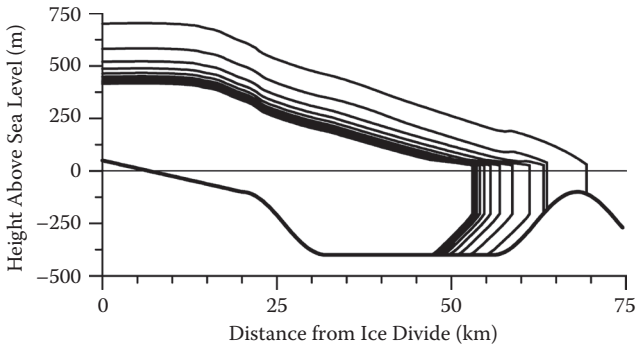


**FIGURE 8.25** Simulated glacier profiles following glacier retreat from the most advanced position with the terminus grounded on the terminal moraine (at 70 km). Profiles are shown every 100 years. (From Nick, F. M. et al., *J. Glaciol.*, 56, 781–794, 2010. Reprinted from the *Journal of Glaciology* with permission of the International Glaciological Society and the authors.)

and, further, result in continued terminus retreat across basal overdeepenings when retreat from the terminal shoal is initiated. In contrast, a crevasse-based calving model allows stable grounding-line positions to be reached, even on a reverse bed slope. Figure 8.25 illustrates this behavior. Starting with a steady-state geometry with the terminus grounded on a terminal moraine (at 70 km), retreat was initiated by decreasing the surface mass balance along the entire glacier length. Terminus retreat is stopped well before the grounding line reaches shallower water, and a new steady state is attained, characterized by the presence of a small floating ice shelf. The formation of this shelf allows the grounding line to advance across basal overdeepenings. Figure 8.26 shows results from a model experiment starting with a

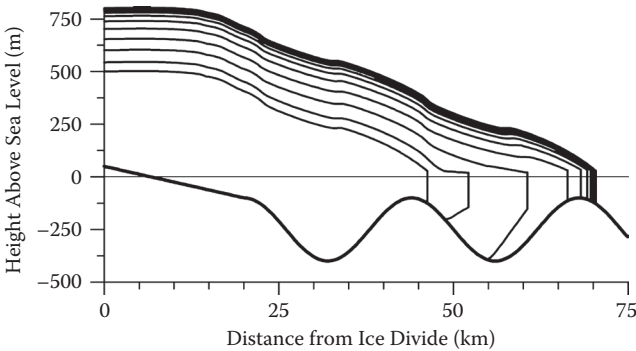


**FIGURE 8.26** Simulated glacier profiles following glacier advance starting with the retracted position with the terminus grounded in shallow water (at 45 km). Profiles are shown every 50 years. (From Nick, F. M. et al., *J. Glaciol.*, 56, 781–794, 2010. Reprinted from the *Journal of Glaciology* with permission of the International Glaciological Society and the authors.)

steady-state profile with the terminus grounded in shallow water (at 45 km). Advance is initiated by increasing the accumulation rate, and a new steady state is reached with the terminus grounded at the terminal moraine (at 70 km).

The results of Nick et al. (2010) demonstrate that the choice of calving model incorporated into time-evolving numerical models determines behavior and stability of the model glacier. Earlier calving models (water-depth and height-above-buoyancy) always produce unstable glacier behavior with retreat of the terminus into deeper water, resulting in continued retreat until shallower water is reached. According to these models, advance across deeper water is possible only if proglacial sedimentation reduces water depth at the grounding line. In the crevasse-penetration models, the calving flux is not directly linked to water depth, and grounding-line dynamics appear to be less sensitive to basal topography (Nick et al., 2010).

A second difference between the crevasse-penetration model and earlier calving models is the ability to reproduce seasonal advance and retreat of the terminus, as observed on Greenland outlet glaciers (for example, Howat et al., 2008; Joughin et al., 2008). Because downward propagation of surface crevasses is directly linked to the amount of water in these crevasses, the rate of iceberg calving increases when surface melting occurs. Consequently, calving rates are greatest during late spring and summer and smallest during the winter, resulting in seasonal retreat and advance of the terminus (Nick et al., 2010). This strong dependency of calving rate on the water level in crevasses was also found by Cook et al. (2012), who noted that this introduces another difficulty in modeling iceberg calving because the water level in crevasses is difficult to determine either through in situ measurements or by using surface mass balance modeling.

The crevasse-penetration calving model applies only to temperate glaciers subject to surface melting. In the absence of water-filled surface crevasses, full thickness fracturing will not occur, nor will surface crevasses be able to reach the waterline. This can be readily shown to be the case by considering a floating ice tongue for which the height above buoyancy,  $H_{ab}$ , equals zero. The combined height of surface and basal crevasses is then

$$d_{\text{tot}} = d_s + d_b = \frac{R_{xx}}{\rho g} + \frac{\rho}{\rho_w - \rho} \frac{R_{xx}}{\rho g} = \frac{\rho_w}{\rho_w - \rho} \frac{R_{xx}}{\rho g}. \quad (8.78)$$

For a free-floating ice shelf, the stretching stress is proportional to the ice thickness, and substituting equation (4.58) into equation (8.78) gives

$$d_{\text{tot}} = \frac{1}{2} H. \quad (8.79)$$

Thus, an additional calving mechanism must be invoked when considering cold Antarctic ice shelves. Bassis and Walker (2012) propose that shear failure may occur on the intact part of the ice thickness separating surface and bottom crevasses (indicated by the dashed line in [Figure 8.24](#)). Their analysis suggests that a floating ice tongue can exist only when the ice entering the terminus region is

relatively intact with few pre-existing crevasses. Another possible mechanism, suggested by Jeremy Bassis (pers. comm., 2012), is that calving may not be determined by crevasse depth estimated from the local stress field, but may be related to deeper crevasses that formed upstream in thicker ice and that are advected to the terminus. As the crevasse moves downglacier, the ratio of crevasse depth to ice thickness increases because the ice thins, while the fracture does not heal or adjust to the altering stress field. Such crevasses could become detachment boundaries for tabular icebergs.

Cuffey and Paterson (2010, p. 127) state that “simulations of calving fluxes in glacier and ice sheet models remain unconvincing.” It is not entirely clear to what models they are referring—their discussion does not include the crevasse penetration model proposed by Benn et al. (2007b) and implemented in a numerical flowline model by Nick et al. (2010). Indeed, a solid theoretical and observational basis for formulating a calving relation is currently still lacking. (Of course, the same can be, and has been, said about the commonly used sliding relation; Fowler et al., 2001.) With regard to the crevasse penetration model, it could be argued that it requires crevasses to remain filled with surface meltwater. Where meltwater is abundant, there is ample evidence that englacial drainage efficiently routes this water to the bed. Moreover, there is little evidence from radar or other measurements that surface and bottom crevasses are co-located or that these can intersect. Finally, as noted above, the crevasse penetration model does not apply where surface melting is mostly absent yet iceberg calving is observed to take place. The main argument in favor of the crevasse penetration model is more heuristic or circumstantial: this model does predict seasonal variations in calving rate and terminus position that appear to be correlated with the onset and intensity of surface melting (as on Columbia Glacier; Tangborn, 1997), and it is based on plausible physical mechanisms.

Establishing a solid foundation for any model of iceberg calving—whether that be the crevasse penetration model or some modification to it, or an entirely different model—remains one of the grand challenges in glaciology. Considering that the choice of calving relation adopted in a numerical model can have a great impact on the behavior and stability of the modeled glacier (Nick et al., 2010), the lack of fundamental understanding of the calving process should be of concern to the glaciological community.